



1 **Contribution of marine biological emissions to gaseous methylamines** 2 **in the atmosphere: an emission inventory based on satellite data**

3 Qi Zhang², Shiguo Jia^{1, 4}, Weihua, Chen³, Jingying Mao⁸, Liming Yang⁵, Padmaja Krishnan⁶, Sayantan Sarkar⁷, Min
4 Shao³, Xuemei Wang³

5 ¹ School of Atmospheric Sciences, Sun Yat-sen University and Southern Marine Science and Engineering Guangdong
6 Laboratory (Zhuhai), Zhuhai, 519082, China

7 ² Tianjin Air Pollution Control Laboratory, Tianjin Academy of Eco-Environmental Sciences, Tianjin, 300191, PR China

8 ³ Guangdong-Hongkong-Macau Joint Laboratory of Collaborative Innovation for Environmental Quality, Institute for
9 Environmental and Climate Research, Jinan University, Guangzhou, 510632, China

10 ⁴ Guangdong Provincial Field Observation and Research Station for Climate Environment and Air Quality Change in the
11 Pearl River Estuary, Guangzhou, 510275, China

12 ⁵ Department of Chemical and Biomolecular Engineering, National University of Singapore, Singapore, 117576, Singapore

13 ⁶ Division of Engineering, New York University Abu Dhabi, Abu Dhabi, P.O. Box 129188, United Arab Emirates

14 ⁷ School of Engineering, Indian Institute of Technology (IIT) Mandi, Kamand, Himachal Pradesh 175075, India

15 ⁸ Scientific Research Academy of Guangxi Environmental Protection, Nanning, 530022, China

16 *Correspondence to:* Xuemei Wang (eciwxm@jnu.edu.cn), Shiguo Jia (jiashg3@mail.sysu.edu.cn)

17 **Abstract.** Methylamines can readily react with acidic gases in the atmosphere, which consequently has an important impact
18 on the atmospheric environment. It is difficult to measure amines in field studies due to their high reactivity, and therefore,
19 numerical modelling is an effective tool to study ambient amines. However, the contribution of marine biological emissions
20 (MBE), an important source of methylamines (MA), has been insufficiently investigated in the current emission inventory.
21 Therefore, this study utilized satellite data such as Sea Surface Temperature (SST), Chlorophyll-a (Chla), Sea Surface
22 Salinity (SSS) and model simulation data (Wind Speed, WS) to establish a more reasonable MBE inventory of amines.
23 Spatial and temporal distribution of methylamine emissions indicates that MBE fluxes of monomethylamine (MMA) and
24 trimethylamines (TMA) can be comparable with or even higher than that of terrestrial anthropogenic emissions (AE), while
25 for dimethylamines (DMA), the ocean acts as a sink. The method used in this study can better reflect the exchange direction
26 of amines between ocean and atmosphere, and reflect the emission characteristics of different amines. From WRF-Chem
27 simulation results, the concentration of amines in the coastline was found to increase significantly due to the contribution of
28 MBE. Wind and Chla were potentially the most important factors affecting MBE fluxes. WS is directly used in the
29 calculation of ocean-atmosphere exchange coefficient K_g , and the direction of the prevailing winds in different seasons
30 affects the area of influence of the MBE. Chla indirectly influences the calculation results of exchange flux by affecting the
31 calculation of pH. In addition, the emission fluxes and spatial distribution of AE and wet deposition also affect the
32 simulation of amines.



33 1 Introduction

34 Amines are derivatives of ammonia, wherein the hydrogen atoms are replaced by hydrocarbon groups. The presence of alkyl,
35 acyl and other functional groups in the amines induces dipole moment effects and makes amines more alkaline than
36 ammonia. Hence, similar to ammonia, amines can readily react with acidic gases in the atmosphere (e.g., gaseous sulfuric
37 acid and organic acids) (Barsanti et al., 2009; Hong et al., 2018; Miao et al., 2018), and can also be substituted for NH_4^+
38 undergoing gas-to-particle phase conversion (Qiu et al., 2011; Qiu and Zhang, 2013; Waller et al., 2018). Amines are known
39 to be important precursors in the nucleation stage during the formation of new aerosol particles in both laboratory
40 experiments and field observations. For example, Elm et al. (2016, 2017) proved that acid–base nucleation requires strong
41 alkaline precursors, with dimethylamines (DMA) and diamines assuming predominance compared to ammonia. Wang et al.
42 (2018) investigated the synergistic effect of methylamine and ammonia during the nucleation process, converting the
43 existing nucleation models from "ternary nucleation" to "quaternary nucleation". Additionally, Yao et al. (2018) indicated
44 based on field observation and CLOUD (Cosmic Leaving Outdoor Droplets) chamber simulations that the " H_2SO_4 –DMA–
45 H_2O " ternary nucleation system may be the primary nucleation mechanism in typical urban areas like Shanghai. Interestingly,
46 Liu et al. (2018) found a strong linear relationship between total amines and NO_3^- in $\text{PM}_{2.5}$, implying that amines mainly
47 exist in the form of aminium nitrate. Lian et al. (2020) recently reported that due to differences in their physicochemical
48 properties, diethylamine (DEA) and trimethylamines (TMA) exhibit variable distributions over different particle types and
49 distinct mixing states; for example, DEA was found to be more associated with sulfate compared to TMA.

50 Generally, amines can be emitted from sources such as animal husbandry, industry, combustion, composting operation,
51 automobiles and other anthropogenic emissions (AE). They are also emitted from natural sources including the ocean,
52 biomass burning, vegetation and geologic processes (Ge et al., 2011). There are about 150 known amines in the atmosphere,
53 including aliphatic amines, amides, aromatic amines, piperazine, pyrrolidine, piperidine, pyrrole, pyridine, pyrazine,
54 quinoline, nicotine, indole, skatole and related derivative amides (Smith et al., 2008, 2010; Loukonen et al., 2010; Barsanti et
55 al., 2009; Ge et al., 2011; Ma et al., 2019; Elm et al., 2016, 2017). Among the above amines, low molecular weight
56 methylamines (popularly referred to as aliphatic amines) containing carbon number in the range of 1–6 are the most
57 abundant species (Ge et al., 2011; Zheng et al., 2015; Yao et al., 2016). Data collected from field observations in urban and
58 mountain sites in southern China showed that monomethylamine (MMA) and DMA were the dominant amines, together
59 contributing to approximately 70% of gaseous amines and 80% of particulate amines (Liu et al., 2018).

60 Globally, ammonia and amines emissions are about 50000 ± 30000 and 285 ± 78 Gg N a^{-1} , respectively (Ge et al., 2011). It is
61 believed that amines have stronger reactivity and are more easily oxidized by oxidants ($\cdot\text{NO}_3$, $\cdot\text{OH}$ and O_3), condensed into
62 particulates and scavenged from the atmosphere by both wet and dry depositions (Carl and Crowley, 1998; Barsanti et al.,
63 2009; Qiu et al., 2011; Qiu and Zhang, 2013; Yu and Luo, 2014; Yao et al., 2016; Mao et al., 2018; Waller et al., 2018). As a
64 result, the concentration of amines in the atmosphere is much lower (usually 3 order of magnitude) than that of ammonia and
65 thus more difficult to be measured (Ge et al., 2011; Yu and Luo, 2014; Yao et al., 2016). For example, the total



66 concentration of MMA, DMA and TMA was 7.4 ± 4.7 pptv, much lower than the concentration of ammonia (1.7 ± 2.3 ppbv),
67 in suburban areas of Nanjing measured during the summer of 2012 (Zheng et al., 2015). The concentrations of C₁–C₆ amines
68 measured by Yao et al. (2016) in the urban areas of Shanghai in the summer of 2015 were 15.7 ± 5.9 , 40.0 ± 14.3 , 1.1 ± 0.6 ,
69 15.4 ± 7.9 , 3.4 ± 3.7 , and 3.5 ± 2.2 pptv, respectively.

70 Typical urban areas along China's east coast have a complex background atmospheric pollution, and in addition to the
71 complex AE from the mainland, the contribution of ocean sources cannot be ignored. Zhou et al. (2019) detected relatively
72 high concentrations of dimethylammonium (DMAH⁺) and trimethylammonium + diethylammonium (TMDEAH⁺) in aerosol samples
73 from Huaniao Island, an ocean site near the Yangtze River Delta, and estimated that marine biogenic emissions (MBE)
74 contributed to 26–31% and 53–78% of aerosol ammoniums over Huaniao Island in the autumn of 2016 and summer of 2017,
75 respectively. Xie et al. (2018) carried out three inland campaigns and one sea-beach campaign in Qingdao, along with five
76 marine campaigns in marginal seas of China and the northwest Pacific Ocean. They observed increased concentrations of
77 DMA⁺ and TMA⁺ in PM_{0.056–10}, particularly, the ratios of DMA⁺/NH₄⁺ and TMA⁺/NH₄⁺ increased by 1–2 orders of
78 magnitude in the marine and sea-beach atmospheres, indicating that the overwhelming majority of amines were derived from
79 marine sources. Further, Hu et al. (2018) linked the significant increase of primary TMA⁺ and secondary DMA⁺ in particles
80 to the emissions of sea-spray aerosols and gaseous precursors from various cyclonic eddies.

81 The atmospheric background in eastern China is generally composed of high concentrations of pollutants and strong oxidants,
82 leading to the formation of secondary pollutants which could be the main reason for the poor air quality (Huang et al., 2014).
83 The secondary gaseous acids, in turn, react with alkaline gases (e.g., NH₃, amines, etc.) and water molecules (H₂O), enabling
84 fast gas-to-particle nucleation, and forming a large number of molecular clusters (Wilemski et al., 1983; Kulmala, 2003;
85 Kirby et al., 2011; Qiu et al., 2011; Qiu and Zhang, 2013; Waller et al., 2018). The rise in aerosol number and mass
86 concentration caused by the formation and subsequent growth of new aerosol particles acts as an impetus for the occurrence
87 of serious haze pollution events in China (Gao et al., 2011; Wang et al., 2014; Xiao et al., 2015; Zhang et al., 2015; Wang et
88 al., 2016; Wang et al., 2017; Wu et al., 2017; Yu, 2011). In addition to the contribution from AE, eastern China's
89 geographical location on the east coast of Eurasia makes it impossible to ignore the impact of MBE. Due to its unique
90 geographical location and pollution composition, eastern China was chosen as the research area in this study.

91 Emission composition and spatiotemporal factors affect the concentration of gaseous amines and the formation mechanism
92 of new particles in polluted areas such as in China. Numerical modelling is an effective tool to study the gaseous amines in
93 the atmosphere. And accurate emission inventories of amines can lead to better model simulations of its atmospheric levels
94 and corresponding spatiotemporal variations, and it in turn can lead to a better understanding of amines' role in atmospheric
95 chemistry and aerosol formation. However, few studies have employed regional and global scale models to simulate gaseous
96 amines and mostly adopted the fixed emission mass ratio of amines to ammonia in the emission inventory (Myriokefalitakis
97 et al., 2010; Yu and Luo, 2014; Bergman et al., 2015). The assumption that the ratio of amines to ammonia emissions is
98 fixed for all emissions is obviously too simplified. Therefore, Mao et al. (2018) derived source-dependent ratios (SDR) that
99 distinguished C₁-amine (CH₃NH₂, also known as MMA), C₂-amine (C₂H₇N, also known as DMA) and C₃-amine (C₃H₉N,



100 also known as TMA) emissions from five different source types (agriculture, residential, transportation, chemical industry,
101 and other industry), which is the most reasonable emission inventory of amines to date. However, the emissions mass ratio
102 obtained was still arbitrary thus leading to high uncertainty in the simulation results. To overcome the arbitrariness of the
103 traditional amine emission inventories, this study establishes an emission inventory of amines including MMA, DMA, and
104 TMA from MBE based on their mechanisms of production. Model simulated wind speed and Multiple satellite datasets
105 including chlorophyll-a, ocean surface temperature and salinity were incorporated to calculate the emission fluxes of amines.

106 **2 Data and Methods**

107 **2.1 Study area**

108 Our study area, shown in Fig. 1, was selected to effectively quantify the impact of MBE in the world's largest ocean, the
109 North Pacific, on China. The selected region encloses longitudes from 85.2° E to 140.8° E and latitudes from 15.4° N to
110 51.9° N. The land area includes most of China, as well as the Korean peninsula and the southern part of the Japanese
111 archipelago. In addition to the Bohai Sea, the Yellow Sea, the East China Sea and the South China Sea, the maritime area
112 also includes the Sea of Japan and parts of the Pacific Ocean.

113 **2.2 Anthropogenic Emission Inventory**

114 Terrain AE inventories are adopted from the Multi-resolution Emission Inventory for China (MEIC)
115 (<http://www.meicmodel.org/>), which was developed by Tsinghua University, and spatially allocated into the 0.25° × 0.25°
116 grid cells. Types of emissions include transportation emissions, residential emissions, other industrial emissions, power
117 plants and agricultural emissions. The primary pollutants mainly include sulfur dioxide (SO₂), nitrogen oxides (NO_x), carbon
118 monoxide (CO), ammonia (NH₃), particulate matter of size less than 10 μm (PM₁₀), particulate matter of size less than 2.5
119 μm (PM_{2.5}), black carbon, organic carbon, and VOCs. To establish the MMA, DMA and TMA emission inventories, we
120 referred to the amines/NH₃ mass emission ratio for different types of emission sources from Mao et al. (2018), which are
121 shown in Table 1. Compared with the previous method where a fixed ratio was used for the total emission sources, the
122 method established by Mao et al. (2018) which provides different ratios for different emission sources has considerable
123 advantages (e.g., it substantially improves the performance of the model in capturing the observed concentrations of MA).
124 However, Mao et al. (2018) also believed that there was underestimation of the ratios they established. Since this study is
125 only a preliminary attempt to explore the contribution of MBE to ambient amines, the method proposed by Mao et al. (2018)
126 is adopted to establish an AE inventory of land-based amines emissions.

127 The emission inventory from marine ships is taken from the Tsinghua University database, with a horizontal resolution of
128 0.25° × 0.25° (Xiao et al., 2018) and pollutants mainly include SO₂, NO_x, CO, NH₃, PM₁₀, PM_{2.5}, black carbon, organic
129 carbon, and VOCs.



130 2.3 Model setup and configurations

131 The online model, WRF-Chem, enables complete online coupling of the chemical module and the atmospheric chemical
132 transport module to simulate trace gas and aerosol emissions, spatial transport, meteorological changes and chemical
133 reactions. WRF-Chem has been widely used in the simulation of air pollutants, and its performance has been widely
134 recognized (Cui et al., 2015; Chen, et al., 2019; Liu, et al., 2017). In this study, WRF-Chem version 3.7.1 was used to
135 simulate the contributions of MBE and AE to amines. Physical and chemical parameterization schemes are shown in Table 2.
136 It should be noted that ambient amines are mainly removed from the atmosphere through the following three ways: i) dry
137 and wet deposition, ii) gas-phase oxidation with oxidizing substances (e.g., $\cdot\text{OH}$, O_3 and NO_x), and iii) aerosol uptake (Yu
138 and Luo, 2014; Bergman et al., 2015). In this study, only the effects of gas-phase reaction and wet deposition on ambient
139 amines concentration were considered in WRF-Chem. As per Yu and Luo (2014), the main oxidant for amines in the
140 atmosphere is $\cdot\text{OH}$, and the effects of O_3 and NO_x are not significant. Therefore, the reaction between amines and $\cdot\text{OH}$ alone
141 was included in the CBMZ gas-phase chemical scheme adopted in this study, and the hydroxyl radical reaction rate constants
142 (K_{OH} , $\text{cm}^3 \text{mol}^{-1} \text{s}^{-1}$) were 2.2×10^{-11} , 6.5×10^{-11} , and 6.1×10^{-11} for MMA, DMA, and TMA, respectively. The wet deposition of
143 amines was treated in the same way as NH_3 .

144 The simulation area is shown in Fig. 1. In the detailed configuration of the model, the centre was set at 28.5°N , 114.0°E ,
145 while the projection was set to Lambert. The year 2015 was chosen as the base year for simulations since it had more
146 consecutive days with field observation (e.g., Zheng et al., 2015; Yao et al., 2016, 2018, etc). January, April, July and
147 October are the representative months of the four seasons in China. However, observation data for gaseous amines for the
148 entire month is unavailable. In this study, observation data from Yao et al. (2018) collected in Shanghai were used for
149 verification, but the data only had daily mean values and some data were missing. Therefore, to understand the seasonality of
150 MBE contributions, the days of four representative months with more consecutive observation data were selected as the
151 simulation period of this study. The observation periods for January (Jan, from 2015.1.1 00:00:00 to 2015.1.10 18:00:00),
152 April (Apr, from 2015.4.8 00:00:00 to 2015.4.17 18:00:00), July (Jul, from 2015.7.22 00:00:00 to 2015.7.31 18:00:00), and
153 October (Oct, from 2015.10.9 00:00:00 to 2015.10.17 18:00:00) with more consecutive data were selected corresponding to
154 winter, spring, summer and autumn, respectively. In addition, the chemical boundary used in this study was modelled using
155 CAM-CHEM as a global simulation result. However, since the chemical species of CAM-CHEM did not contain amines, the
156 three amines involved in this study, MMA, DMA and TMA, were obtained based on their mass ratio with ammonia, which
157 were 8.5×10^{-4} , 1.56×10^{-3} and 3.7×10^{-4} , respectively (Zheng et al., 2015). More specific information is available at
158 <https://www.acom.ucar.edu/cam-chem/cam-chem.shtml>. Biogenic emissions were calculated online using MEGAN
159 (Model of Emissions of Gases and Aerosols from Nature) coupled in the WRF-Chem (Guenther et al., 2006).



160 2.4 Calculation of air–ocean net exchange flux of methylamines

161 Part of ammonia and methylamines dissolved in seawater exist as solvated cations due to ionization (e.g., NH_4^+ , MMAH^+ ,
162 DMAH^+ , TMAH^+), accounting for >90% of the total dissolved ammonia and amines in seawater (Carpenter, et al., 2012). In
163 addition, there are a small number of unionized gas molecules (e.g., NH_3 , CH_3NH_2 , $(\text{CH}_3)_2\text{NH}$, $(\text{CH}_3)_3\text{N}$) that can be
164 exchanged between the atmosphere and the ocean (Carpenter, et al., 2012), and the net fluxes of ammonia and amines across
165 the interface can be calculated from the following equation (Liss and Slater, 1974):

$$166 F = K_g ([C_{(g)}] - H[C_{(s)}]) \quad (1)$$

167 Where, F is the gaseous interfacial flux between air and ocean ($\text{pmol m}^{-2} \text{ s}^{-1}$); $C_{(g)}$ is the concentration of gas (nM; e.g.,
168 $\text{NH}_{3(g)}$, $\text{MMA}_{(g)}$, $\text{DMA}_{(g)}$, $\text{TMA}_{(g)}$) determined by the measurement carried by Gibb et al., (1999); Table 3); $C_{(s)}$ is the
169 corresponding concentration of unionized solute molecules (nM); K_g is the air–ocean transfer velocity (m s^{-1}); H is the
170 dimensionless Henry's Law constant (the ratio of the partial pressure of the gas to the amount of gas dissolved in a
171 quantitative liquid at a certain temperature at equilibrium). The Henry's Law constant, H , depends on the temperature (T , °C)
172 and the ionic strength (I , mol dm^{-3}) of seawater. For NH_3 , H is calculated from Eq. (2). In this study, H of amines was also
173 calculated based on Eq. (2) (Gibb et al., 1999).

$$174 H = \left[28.0 \exp \left(\ln K_{H(293)} - \frac{4092dT}{T^2} \right) \right]^{-1} \quad (2)$$

175 K_H (M atm^{-1}) represents the temperature dependence of H for transfer between the gaseous and liquid phases (Gibb et al.,
176 1999).

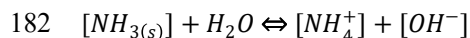
$$177 \ln K_H = 4092/T - 9.70 \quad (3)$$

178 The calculation of K_g is shown below (Duce et al., 1991),

$$179 K_g = \frac{U}{770 + 4.5MW^{1/3}} \quad (4)$$

180 Where, MW is the molecular weight of the gas (g mol^{-1}), and U is wind velocity (m s^{-1}).

181 Solute molecules of ammonia and amines generally have the following ionization equilibrium in seawater (e.g., ammonia),



183 The corresponding base dissociation constant (K_b) is calculated as follows:

$$184 K_b = \frac{[\text{NH}_{4(s)}^+][\text{OH}^-]}{[\text{NH}_{3(s)}]} \quad (5)$$

185 Consequently, Eq. (6) can be used to calculate the concentration of $C_{(s)}$ (Van Neste et al., 1987),

$$186 [C_{(s)}] = \frac{[C_{(s)tot}^+][\text{OH}^-]}{K_b + [\text{OH}^-]} \quad (6)$$

187 Where $[C_{(s)tot}^+] = [C_{(s)}] + [C_{(s)}^+]$, is the total dissolved concentration of analyte (nM, i.e. $\text{NH}_{4(s)tot}^+$, $\text{MMAH}_{(s)tot}^+$, $\text{DMAH}_{(s)tot}^+$,
188 $\text{TMAH}_{(s)tot}^+$), $[C_{(s)}^+]$ is the concentration of corresponding solvated cation (nM, e.g. $\text{NH}_{4(s)}^+$, $\text{MMAH}_{(s)}^+$, $\text{DMAH}_{(s)}^+$,
189 $\text{TMAH}_{(s)}^+$). Since the data of amine dissolution in surface waters near the eastern coastal areas of China are scarce, this study
190 selected the average of the observed values of other sea areas (Table 3). Nakano and Wakanabe's (2005) research showed the



191 spatio-temporal distribution diagram of marine environmental parameters (sea surface temperature (SST), Chlorophyll a
192 (Chla), and pH) in the North Pacific Region. The results showed that marine environment near the mainland and marine
193 parameters are affected by the climate zone they are located in as well as the human activities near the coast. The eastern
194 coastline of China spans multiple temperature zones and the economic activities and concentrated population near the coastal
195 areas result in higher pollutant emissions. Therefore, observations at a single site cannot represent the dissolution of amines
196 in surface seawater off the eastern coastal areas of China. The research data listed in Table 3 are respectively from the
197 Pacific Ocean, Indian Ocean and Atlantic Ocean, corresponding to temperate, subtropical and temperate zones, respectively,
198 and all sites are located in densely populated areas. Therefore, the average of these studies is assumed as the concentration of
199 total dissolved amines. Hydroxide ion concentration ($[OH^-]$) in Eq. (6) can be calculated based on the measured pH,

$$200 [OH^-] = 10^{-(14-pH)} \quad (7)$$

201 Since this study is mainly focused in the Pacific region, which has a significant impact on the southeast coast of China, we
202 adopted a simple function for pH calculation proposed by Nakano and Watanabe (2005), which is applicable to the surface
203 seawater over the North Pacific Basin for all seasons, and is related to SST (same as T , K) and $Chla$ ($mg\ m^{-3}$),

$$204 pH_{p(T)} = -0.00266SST - 0.0243Chla + 8.892 \quad (8)$$

205 The dissociation constant K_b in Eq. (5) is calculated from the corresponding stability constant, pK_a ,

$$206 K_b = 10^{-(14-pK_a)} \quad (9)$$

207 Further, K_a is also dependent on the temperature and ionic strength. For the $NH_{3(s)}-NH_{4^+(s)}$ system, the calculation of pK_a can
208 be obtained from the empirical equation provided by Khoo et al. (1977) and applicable when the water salinity is within 45:

$$209 pK_a = pK_{wa} + (0.1552 - 0.003142 T)I \quad (10)$$

210 Where, pK_{wa} is the value of pK_a in the pure water ($T=20\ ^\circ C$, $I=0\ mol\ dm^{-3}$). The relationship of pK_a with T and I (Eq. (11)),
211 is also assumed for the amines. Gibb et al. (1999) has confirmed the usability of this method in the Arabian Sea and the
212 detailed information of the physicochemical parameters used in the above calculations are summarized in Table 4. Ion
213 intensity (I) can be calculated from the measured sea surface salinity (SSS) using the following equation (Lyman and
214 Fleming, 1940),

$$215 I = 0.00147 + 0.01988 SSS + 2.08357 \times 10^{-5} SSS^2 \quad (11)$$

216 2.5 Data Used in the Calculation

217 To calculate net exchange flux of methylamines between air and ocean, the key is to calculate the concentration of amines
218 dissolved in seawater. As a class of soluble organic bases, the dissolution and ionization equilibrium of MMA, DMA, and
219 TMA are closely related to the pH of seawater. Therefore, in this study, high-precision satellite data were used and the
220 algorithm suitable for the north Pacific region proposed by Nakano and Watanabe (2005) was employed to calculate the
221 high-precision spatial and temporal distribution of pH data of the studied marine region.



222 2.5.1 Sea Surface Temperature

223 SST is one of the most important variables in marine hydrological conditions. It can directly or indirectly affect MBE of
224 amines by influencing biological and physicochemical processes in the ocean. The global high-resolution satellite-based
225 daily mean SST data used in this study was released by NOAA's National Environmental Satellite Data and Services
226 (NESDIS) office, with a resolution of 0.05° ($\sim 5\text{km}$) and within operational bias. The SST data was combined with analysis
227 from the US, Japanese and European Synchronous Infrared Imagers and Low Earth Orbit Infrared (US and Europe) to
228 produce a set of high-resolution (5km) SST data products. The grid scale was chosen to achieve a resolution close to the
229 Nyquist sampling standard of the Rossby radius ($\sim 20\text{ km}$) at mid-latitudes to preserve mesoscale oceanic features such as
230 vortices and frontal meanders. The input SST data itself is also internally processed using the Geo-SST Bayesian and
231 physical retrieval methods (GOES-E/W, Meteosat-10). For polar orbits and Himawari-8, the Advanced Clear Sky Processor
232 for Oceans (ACSPO) is adopted. More detailed information is available at [https://coastwatch.noaa.gov/cw/satellite-data-](https://coastwatch.noaa.gov/cw/satellite-data-products/sea-surface-temperature/sea-surface-temperature-near-real-time-geopolar-blended.html)
233 [products/sea-surface-temperature/sea-surface-temperature-near-real-time-geopolar-blended.html](https://coastwatch.noaa.gov/cw/satellite-data-products/sea-surface-temperature/sea-surface-temperature-near-real-time-geopolar-blended.html). The SST data has been
234 updated since 2019. In this study, the average of the same month in the simulation period was selected for calculation. The
235 specific spatial and temporal distribution is shown in Fig. 2(a, b, c, d). SST presents the seasonality of July > October > April
236 > January. In terms of spatial distribution, the SST of Bohai Sea and Yellow Sea in China is lower than that of sea areas with
237 the same latitude in spring and winter, which may be due to the fact that it is controlled by continental high in spring and
238 winter, and the prevailing northwest dry and cold monsoon, leading to low temperature. Similarly, this can also explain the
239 low SST in the coastal areas, and with the decrease of latitude, the influence of the continental high gradually decreases,
240 which is similar to that in the sea areas of the same dimension in Guangdong, Hainan and other provinces.

241 2.5.2 Chlorophyll-a

242 The Ocean Color Satellite Sensor measures visible light at specific wavelengths that leave the ocean surface and reach the
243 top of the atmosphere where the sensor is located. Measurements of these visible spectra, along with simultaneous
244 measurements of near-infrared (NIR) and short-wave infrared (SWIR) wavelengths, can be used to calculate ocean color or
245 standardized radiation out of water (nLw). In turn, $nLws$ can be used to derive other marine properties, such as the
246 concentration of Chla (chlorophyll is mainly used for photosynthesis, so it can be used as an important indicator of
247 phytoplankton biomass in seawater) and the extinction coefficient of infiltration irradiation ($K_d(\text{PAR})$ and $K_d(490)$, which
248 are related to the purity of seawater). The Chla datasets used in this study were obtained from the Visible and Infrared
249 Imaging Radiometer Suite (VIIRS) sensors on the Suomi-NPP satellite (SNPP) launched in November 2011, and the
250 NOAA-20 satellite launched in November 2017. NOAA marine color data is processed using the NOAA Multi-Sensor Level
251 1 to Level 2 Processing System (MSL12). The system was developed by the NOAA/STAR Marine Colour Team. Further
252 details on the datasets are available at <https://coastwatch.noaa.gov/cw/satellite-data-products/ocean-color/near-real->



253 time/viirs-multi-sensor-gap-filled-chlorophyll-dineof.html. The data has been updated since 2018. In this study, the average
254 of the same month in the simulation period was selected for calculation.

255 As can be seen from Fig.2(e, f, g, h), the seasonality showed a trend of October > April > July > January. The reason of the
256 specific spatial and temporal distribution is that temperature gradually increased in April, and upwelling lead to the delivery
257 of nutrients to the at the ocean surface, which translates into plankton growth and corresponding increase in Chla. However,
258 with the further increase of temperature in July, fish, shrimp and other benthic organisms in the ocean gradually enter the
259 breeding period, and a large number of larvae feed on plankton, thus resulting in a decrease in Chla due to the increase in the
260 consumption of plankton. In October, the consumption of plankton by the larvae of marine organisms decreased. In addition,
261 a large amount of nutrients were accumulated in the sea water in July, and plankton began to multiply in large numbers.
262 Therefore, the highest Chla value appeared in autumn. Then in winter (January), the temperature of sea water decreased and
263 the life activities of plankton weakened, and therefore Chla decreased. In addition, from the perspective of spatial
264 distribution, the seasonality of Chla in the offshore area is more obvious, while the seasonality in the pelagic area is not
265 obvious. High values of Chla are mainly distributed in the offshore areas, and also appear in the areas far from the land in the
266 East China Sea in spring. On the one hand, human activities discharge nutrients into the ocean from the estuaries of Liaohe
267 River, the Yellow River, Huaihe River, the Yangtze River and the Pearl River. In addition, the fishing grounds of Yellow-Bo
268 Sea, Zhou-Shan, south China sea coast and Beibu Gulf Fisheries, which distribute from north to south, lead to a coastal input
269 of increased nutrients, so plankton blooms in the coastal areas. On the other hand, at the estuary of rivers, the difference in
270 salinity between fresh water and sea water causes sea water to churn, hence, sea water turbidity increases, reducing the
271 intensity of light and restricting the growth of plankton. As the sea water moves outward, its vertical stability increases, the
272 sediment deposition and the transmittance increase, which results in phytoplankton multiplication in large numbers, and a
273 high value of Chla appears again in the pelagic area of the East China Sea (Zhang et al., 2016).

274 2.5.3 Sea Surface Salinity

275 The SSS data used for ion intensity (I) calculation started in April 2015, when the level-3 grid-based SSS daily mean data set
276 with spatial resolution of 0.25° was obtained from observation and inversion by SMAP (Soil Moisture Active Passive)
277 satellite. Coast Watch/ Ocean watch Level-3 SSS products are generated directly from the NASA Jet Propulsion Laboratory
278 (JPL) SMAP Level-2B SSS near real time SWATH HDF5 file. These products improve the application of satellite SSS
279 products, to reduce data delay to 24 hours (<https://coastwatch.noaa.gov/cw/satellite-data-products/sea-surface-salinity/smap.html>). In this study, the data of April, July and October 2015 were adopted as the average of the research
280 period, while the missing data of January 2015 were replaced by the data of January 2016. As can be seen from Fig.2 (i, j, k,
281 l), the seasonality of SSS was April > July > January > October. This is mainly because the value of SSS can be affected by
282 precipitation, evaporation, fresh water input from outflow river and tidal action. From spring (April) to summer (July),
283 precipitation in the southeast coastal areas of China gradually increases, and the amount of water input from estuaries also
284 greatly increases, leading to a gradual decrease in SSS, which reaches the lowest value in autumn (October). Then in the
285



286 autumn, the precipitation begins to decrease, and SSS also begins to rise gradually, and reaches peak again in the spring of
287 the next year. The seasonality of SSS in the East China Sea is obvious, mainly because it is significantly affected by the
288 Yangtze River, and SSS is inversely proportional to the runoff input. However, in the South China Sea and east of Luzon
289 Island, the variation of SSS is not obvious, which is mainly related to the climate characteristics of high temperature and
290 rainy periods all year round in this region (Liang et al., 2019).

291 **2.5.4 Wind Speed**

292 Due to the lack of wind speed (WS) data with high temporal and spatial resolution, and issues of data integrity, the WS used
293 in this study was simulated by WRF based on FNL forecast data. Table S1 shows the comparison between the simulated
294 results and the observed values of meteorological elements. It can be seen from the results that the model can simulate the
295 numerical values and variation trends of WS, temperature and relative humidity.

296 It can be seen from Fig. 2 (m, n, o, p) that the wind speed is strongest in winter (January), weakest in summer (July) and
297 transitions from spring to summer, which is also consistent with satellite data reported in other studies (Lin et al., 2000). The
298 wind blows from the ocean to the land in summer, and from the land to the sea in spring, autumn and winter, which also
299 causes the land to be affected by more MBE in summer.

300 **3 Results and Discussion**

301 **3.1 Spatial and temporal distribution of methylamines emissions**

302 The emission fluxes of the three types of amines in January, April, July and October are shown in Table 5. Negative values
303 indicate that the amine is transported from the ocean to the atmosphere, where the ocean is the source of the amine. Positive
304 values indicate that amines are transported from the atmosphere to the ocean, which is a sink of amines. To facilitate the
305 comparison with terrestrial AE, the positive and negative signs were adjusted in this study. The positive values of the
306 original calculation results were changed to negative values, indicating that the ocean is the sink. A change in the negative
307 value of the original calculation to a positive value indicates that the ocean is the source. The established spatial and
308 temporal distribution of the amines emissions is shown in Fig. 3, and the diurnal variation of the emission flux is shown in
309 Fig. 4. As we can see, the MBE fluxes of amines are quite substantial. The MBE emission fluxes of MMA are close to
310 terrestrial AE in January and October, but is relatively low compared with terrestrial AE in April and July. TMA was higher
311 in January and October, but lower in April and July. Overall, TMA was significantly higher than terrestrial AE. The peak
312 value of terrestrial AE is concentrated between 4:00 and 8:00. Due to the relative stability of the marine environment, the
313 diurnal variation range of MBE is not as obvious as that of terrestrial AE, but it can still be seen from Fig. 4 that the MBE
314 have a slight increase in the daytime.

315 The influence of the four variables on the exchange fluxes is shown in Fig. 5. As shown in Eq. (4), WS is directly used in the
316 calculation of ocean-atmosphere exchange coefficient K_g , which is directly proportional to K_g , and has the most direct



317 influence on the calculation of exchange fluxes. Higher WS will accelerate the material exchange between the ocean and the
318 atmosphere, which is directly reflected in the change of the exchange fluxes, and the two show a significant linear
319 relationship (Fig. 5(a)). For MMA and TMA, the ocean is the source, and the increase of WS will lead to a linear increase in
320 the emission fluxes. For DMA, the ocean is a sink, and the increase in WS also accelerates the flow of atmospheric DMA
321 into the ocean. The other three variables have an indirect effect on the exchange fluxes mainly by affecting the calculation of
322 intermediate variables.

323 With the increase of Chla, the direction of amines exchanges between the ocean and atmosphere showed a trend of
324 transferring from the atmosphere to the ocean (Fig. 5 (b)). According to Eq. (9), the increase of Chla will lead to the decrease
325 of pH, hence, it is not conducive to the overflow of amines. Chla is used to indicate primary production in the water body,
326 and high Chla indicates a significant increase in phytoplankton in the water body. Water eutrophication is caused by the
327 massive growth of phytoplankton due to the continuous importation of anthropogenic nutrients into the sea by rivers. Thus,
328 the increased organic matter is transported to the subsurface water by settling and being decomposed by microorganisms.
329 This process consumes oxygen in the water and forms a hypoxic environment. With the mixing of the water, the pH of the
330 water changes. Zhao et al. (2020), based on the observation data of summer voyage from the Pearl River Estuary to the
331 northern continental shelf of the South China Sea, found that the water on the west side of the Pearl River Estuary with
332 obvious mixing of fresh water and seawater is characterized by low dissolved inorganic carbon (DIC) and high pH, while for
333 the area with 20-30 meters water depth outside the mixing area, it is characterized by high DIC and low pH. The main source
334 of amines comes from the degradation of organic matter in sediments, therefore, an increase in Chla might mean more
335 acidification in the ocean, making amines more soluble in seawater.

336 An increase in SST will also lead to a decrease of the fluxes of amines discharged from the ocean to the atmosphere (Fig. 5
337 (c)). As can be seen from Eq. (9), the increase of SST will lead to the decrease of pH, which is not conducive to the overflow
338 of amines. Due to the high stability of the marine environment, the variation range of SST itself is small, hence, SST has the
339 least influence on the exchange flux among the four elements. It should be noted that, El Niño conditions occurred by late
340 May in 2015, which increased the global average temperature and affected the weather patterns in the study area (Kennedy et
341 al., 2016). The annual average SST of our study areas was 0.5-1.0 °C higher than the average value recorded during the
342 period from 1961 to 1990 (Kennedy et al., 2016). Figure 5(c) shows that the exchange fluxes of amine are positively
343 correlated with SST, but the sensitivity is low.

344 It can be seen from Fig. 5 (d) that the increase of SSS will increase the tendency of the amines to overflow the water surface.
345 It can be inferred from Eq. (9), (10), (11), and (12) that the increase of SSS will further inhibit the ionization of amine in
346 seawater, which makes it more prone to overflow from the water surface, resulting in an increase of the exchange fluxes.
347 However, in general, WS and Chla are the main factors affecting the exchange fluxes.



348 3.2 Spatial and temporal distribution of methylamine concentrations

349 Due to the temporal and spatial resolution of the model and the incompleteness of observation data, it is not possible to
350 directly compare the model simulation results with the observation data in this study. But on the whole, the simulated results
351 of amines are close to their actual concentrations in the atmosphere in terms of magnitude, and inclusion of marine biogenic
352 emissions can make up for the shortcomings of the previous models' underestimation of amines. Table 6 summarizes the
353 amine concentrations for this study and data from other published papers (both simulation and measurement data).
354 Considering the large simulation area and low grid resolution in this study, the Yangtze River Delta region with relatively
355 dense observation sites was selected to verify the calculation results effectively. Without considering the contribution of
356 MBE, the simulation results in this study accord with the general rule of DMA>MMA>TMA, which can be attributed to the
357 difference in AE fluxes. Previous simulations often underestimated the amines concentration (Mao et al., 2018). The
358 contribution of MBE to TMA and MMA will effectively improve the regional simulation value. Moreover, due to the
359 increased consumption of ·OH by TMA and MMA, the consumption of DMA will decrease and the average concentration
360 will increase slightly in the spring and summer when the photochemical reaction is strong. However, there was no significant
361 change in the range in autumn and winter (Table 6). Figures 6, 7, and 8 show the spatial and temporal distribution of the
362 simulated concentrations of the three amines in the presence and absence of MBE. Due to the contribution of MBE, the
363 ambient concentration of TMA of coastal areas increased multiple times, and the concentration of amines above the offshore
364 area also increased significantly. The specific amount of increase is shown in Table 6. In January, April, July and October,
365 TMA increased by 37.1%, 23.7%, 36.5% and 27.9%, respectively, while TMA increased by more than 10% in the area over
366 500 km from the coastline. The increase rates of TMA in the four months even reached 229.6%, 107.1%, 116.7% and
367 171.5%, with significant increases over Bohai Bay, Yangtze River Delta, Leizhou Peninsula and the Sea of Japan. The
368 second is MMA, with an average increase rate of 4.0%, 3.7%, 7.8% and 3.6% in January, April, July and October,
369 respectively. The increase of MBE mainly affects the area about 50 kilometers from the coastline. In the four months, the
370 average increase rates of MMA in this part reached 57.9%, 23.9%, 26.2% and 37.5%, with considerable increases over
371 Bohai Bay, Yangtze River Delta, the waters around Leizhou Peninsula and the Sea of Japan. Moreover, due to the obvious
372 increase of the other two amines, ·OH decreased and the consumption of DMA decreased correspondingly, thus leading to a
373 small increase in the DMA concentration. The seasonality of MMA and TMA increases is consistent with the seasonality of
374 emission fluxes (January > October > April > July).

375 As can be seen from the above description, WS could be the most important factor affecting MBE fluxes because it is
376 directly used to calculate the air-ocean exchange coefficient (K_g) (Eq. (4)). At the same time, wind direction is another
377 important factor that affects MBE. In July, the monsoon blows from the sea to the land, causing the effects of MBE to reach
378 deep into China's interior. It can also be seen from Figures 6, 7 and 8 that the concentration of amine over land in July
379 changed the most. Furthermore, the influence of MBE is also conditioned by the monsoon and the topography of China.
380 Specifically, the terrain of China can be divided into three steps: the low east, the high west and the third step extending to



381 the ocean. The third step, i.e., the offshore continental shelf, is usually the region less than 500 meters above sea level, and is
382 most affected by MBE. Moreover, the influence of MBE on western China is weakened due to the barrier between the
383 second and third steps (Mt. Greater Hinggan–Mt. Taihang–Mt. Wushan–Mt. Xuefeng). Therefore, the prevailing southwest
384 monsoon in July can smoothly drive the marine air mass into the third step area, and its influence area is wider due to the
385 lack of obstacles in the north-south direction. However, in January, April and October, the prevailing northerly monsoon
386 brings more terrestrial air, limiting the contribution of MBE. The geographical location also has an important influence on
387 the MBE contribution. Some regions are always affected by the strong ocean air mass. For example, Hainan Island and the
388 Shandong Peninsula are surrounded by the sea on many sides, hence, they are affected by strong oceanic air mass during all
389 four seasons. Moreover, Southern China (especially, the coastal areas of Fujian and Guangdong provinces) is more affected
390 by MBE than northern China due to the prevailing winds blowing from the sea to the land.

391 Moreover, it should be noted that after the addition of MBE, not all regions showed an increase in the concentration of
392 amines; some regions showed a small decline. However, compared with the increase, the decrease was not significant. Even
393 in July, when the ocean source had the greatest influence, the average concentration in the drop area was lower than 10%
394 (Table 7). This situation may be caused by the reaction equilibrium of $\cdot\text{OH}$ and NO_x in the atmosphere which is affected by
395 MBE. If MBE are added, $\cdot\text{OH}$ consumption will take place, and photolysis of HONO will be promoted to generate more NO.
396 However, NO will react with $\cdot\text{OH}_2$ at a faster reaction rate to generate $\cdot\text{OH}$, which will lead to an increase in $\cdot\text{OH}$
397 concentration in some areas. In the upwind region, the amine is consumed and cannot be replenished enough, which leads to
398 the decrease of the amine concentration in some areas after the increase of MBE.

399 3.3 The main factors affecting amines simulation

400 The simulation of amines is mainly influenced by two factors, namely the emissions and model mechanism. Therefore, this
401 study designed sensitivity tests from the two aspects, and discussed the contribution of different types of terrestrial AE to
402 amines, the data used to calculate MBE and the influence of wet deposition on the simulation of amines.

403 3.3.1 Terrestrial anthropogenic emissions

404 The contributions of different terrestrial AE to amines concentration were significantly different. As shown in Table S2,
405 agricultural emission is the major source of the three types of amines. However, the agricultural emissions of DMA are
406 relatively low compared with the agricultural emissions of MMA and TMA accounting for more than 80%. Residential
407 emission is another important source of DMA, accounting for more than 10% in each of the four months, and even reaching
408 36.5% in January. Industrial emission is the third major source of amines, accounting for about 5%. The contribution of
409 transportation emissions is very low (<1%), and the contribution of power plant emissions is negligible. In addition, the
410 contribution ratio of different emissions also presents a strong seasonality. Due to the wide distribution of agricultural
411 emissions and the absolute dominance among all kinds of emissions, this study only conducted sensitivity tests on residential



412 emissions and industrial emissions, i.e., quantitative analysis was conducted on the change of amines concentration after the
413 complete removal of a certain type of emissions.

414 Fluxes and spatial distribution of different emissions will affect the amines concentration. After the reduction of residential
415 emissions, DMA showed stronger sensitivity than the other two amines due to residential emissions' high proportion in the
416 total emission of DMA. After the reduction of industrial emissions, the changes of the three amines were not different from
417 each other and were consistent with the reduction of emissions (~5%). However, the spatial distribution of residential and
418 industrial emissions make the change of amines simulated concentration significantly different (Fig. S1). As can be seen
419 from Fig. S2 and S3, residential emissions are distributed in a wide range. Although like agricultural emissions, they have
420 relatively high fluxes in areas such as Sichuan Basin, North China Plain, Yangtze River Delta and Pearl River Delta, the
421 difference is not obvious. Therefore, the decrease range of amines concentration is approximately uniform in the simulated
422 region. The industrial emissions are concentrated in the north of the Yangtze River, especially in Shandong, Shanxi, Shaanxi,
423 Henan, Hebei, etc., and there is a significant difference between the high value area and the low value area. Therefore,
424 although the proportion of the total industrial emissions are not high, the local decline caused by the reduction is relatively
425 high, and the influence is greater mainly in the places where industrial emissions distribution is more concentrated.

426 3.3.2 Marine biological emissions

427 To further explore the influence of satellite data on the spatial distribution of the simulated amines concentration, two
428 variables, Chla and WS, which have obvious effects on the emission flux of amines, were selected and sensitivity tests were
429 conducted by increasing or decreasing the values by 50%. SSS and SST were not considered due to their small variation
430 range and small influence on the amines exchange fluxes.

431 The concentration change of Chla is related to the calculation of pH, hence, it has an indirect effect on the calculation of the
432 emission flux of amines. When Chla decreased, the pH of seawater would rise to a certain extent, which would promote the
433 overflow of amines from seawater. With the increase of Chla, the pH of seawater will show a downward trend, which will
434 inhibit the overflow of amines. After increasing or decreasing Chla, the maximum variation ranges of seawater pH in
435 January, April, July and October were ± 0.27 , ± 0.52 , ± 0.56 and ± 0.70 , respectively. The higher the concentration of Chla, the
436 more obvious was the pH change caused by it, which was mostly concentrated in the coastal areas. In addition, it can be seen
437 from the discussion in Section 3.1 that the influence of Chla on emission fluxes gradually decreases with the increase of Chla
438 and eventually tends to stabilize. Therefore, the effect of Chla reduction on emission fluxes is higher than that of Chla
439 increase, as can be clearly seen from Table S3. Moreover, the effect of Chla on MMA is significantly higher than that of
440 TMA, mainly because MMA is more alkaline, thereby making it more sensitive to changes in pH.

441 From Fig. S4 and Fig. S5, we can see the spatial and temporal changes of the final simulated values of amines after reducing
442 and increasing 50% Chla. The influence of Chla variation is mostly concentrated in the maritime area and the area adjacent
443 to the coastline (<27km), and the magnitude of the influence is directly related to the variation range of amines emissions.



444 Except for July, the impact on land is small, and the fluctuation is generally less than 5%. In July, due to prevailing winds
445 blowing from the ocean to the land, the amine variation is greater (>5%). In addition, although the change of MBE of DMA
446 is not considered here, the changes of MMA and TMA have an impact on the reaction cycle of $\cdot\text{OH}$, which indirectly affects
447 the concentration of DMA. The range of DMA over land is like that of TMA and MMA, but the effect over the ocean is
448 mainly downwind of the prevailing wind direction. This phenomenon is mainly caused by the fact that the reactivity of DMA
449 is higher than that of TMA and MMA; therefore, DMA reacts with $\cdot\text{OH}$ faster than the other two amines in the upwind
450 direction, and its concentration is less affected. However, as time goes on, the effect of TMA and MMA concentration
451 changes becomes prominent, and DMA changes greatly downwind of the prevailing wind direction.

452 There is a positive linear correlation between WS and the emission fluxes. Thus, a 50% reduction or increase in WS is
453 equivalent to a 50% reduction or increase in the overall MBE. Similar to the results obtained from changing Chla, changing
454 WS mainly had a significant effect on the concentration of amines over the sea, and the effect on land was mainly confined
455 to the coastal areas. In the example of the 50% reduction of WS (Fig. S6), for MMA and TMA, the 50% reduction of MBE
456 resulted in significant changes in the simulated values of both over the ocean. Moreover, due to the prevailing wind blowing
457 from land to sea in January, April and October, the changes of these two amines over the land were not obvious. In July, due
458 to the prevailing wind blowing from the ocean to the land, the change of MBE has a greater impact on the land. However,
459 there are still differences between the two. As the MBE fluxes of MMA are slightly lower, the amine concentration in the
460 offshore area near the land can be supplemented by AE, so the reduction of the amine concentration in the offshore area is
461 relatively small, and it is obvious in January, April and October. However, due to the higher fluxes, TMA is more sensitive
462 than MMA, and the supplementary effect of terrestrial AE on TMA over the offshore area is not obvious.

463 3.3.3 Wet Deposition

464 Like ammonia, amines are considerably soluble in water, and hence the influence of wet deposition on the simulated
465 concentration of amines cannot be neglected. As seen from Fig. S7, the cumulative precipitation presents great differences in
466 different simulation periods. In the simulation period of January, April and October, the precipitation was low, going below
467 50 mm in October. However, in July, there is significant precipitation and an obvious rainfall zone between Jiaodong
468 Peninsula and Guangdong province. This temporal and spatial distribution must have different effects on the concentration
469 of amines. To explore the influence of wet deposition on the simulation of amines, the apparent Henry constant of amines in
470 the model was set as 0.75 times and 1.25 times of the original, respectively. The larger the apparent Henry coefficient, the
471 easier it is for the amine to dissolve in precipitation and be removed from the atmosphere.

472 It was found that with the decrease of the apparent Henry coefficient, the amines became more difficult to dissolve in water,
473 and therefore, the concentration of amines increased in most areas (Fig. S8). However, in January, April and October, the
474 variation of amine concentration over land during the simulation period was generally small due to lower precipitation.
475 DMA is only affected by terrestrial AE, and when its concentration over the land increases, it is carried to the atmosphere
476 over the sea under the action of prevailing wind. As a result, the variation range of its concentration over the sea surface is



477 significantly higher than that of the other two amines, and the affected area is mainly concentrated in the downwind area of
478 the prevailing wind. In July, due to more precipitation, the effect on amines was significantly stronger than that in other
479 months. In addition, the area with more obvious change coincides with the rainfall zone mentioned above. Moreover, the
480 transport of prevailing winds from the ocean to the land and the blocking effect of the mountains dividing steps two and
481 three in the east made the whole eastern coastal area exhibit the most obvious change in the concentration of amines. When
482 the Henry's coefficient is increased, the trend is reversed.

483 **4 Conclusions**

484 In this study, numerical modelling was employed to calculate amine emissions from ocean sources by using satellite data
485 such as SST, Chla, and SSS. Algorithms were used to establish a more reasonable MBE contribution for the amines
486 including C₁-amine (CH₅N, MMA), C₂-amines (C₂H₇N, DMA) and C₃-amines (C₃H₉N, TMA). The ocean acts as the source
487 for MMA and TMA in all seasons and acts as a sink for DMA. However, if the traditional ratio method is adopted, whether
488 the ocean is the source of amine emission depends entirely on whether ammonia can be discharged from the ocean. This
489 "one-size-fits all" method is not consistent with the actual situation, and further affects the simulation results of subsequent
490 models. The satellite data used in this study can better reflect the exchange direction of amines between ocean and
491 atmosphere and reflect the emission characteristics of different amines, which is more consistent with the reality.

492 The calculated spatial and temporal distribution of methylamine revealed that MBE can effectively increase the amines
493 concentrations in most areas. Due to the contribution of MBE, the ambient concentration of TMA of coastal areas increased
494 multiple times, and the concentration of amines above the offshore area also increased significantly. TMA increased by more
495 than 10% in the area over 500 km from the coastline. The increase rates of TMA in four months reached 229.6%, 107.1%,
496 116.7% and 171.5%. The next largest increase was observed for MMA, with an average increase rate of 4.0%, 3.7%, 7.8%
497 and 3.6% in January, April, July and October, respectively. The increase of MBE mainly affects the area about 50 kilometers
498 from the coastline. In the four months, the average increase rates of MMA in this part reached 57.9%, 23.9%, 26.2% and
499 37.5%. WS and Chla were found to be the dominant factors affecting MBE fluxes. WS is directly used in the calculation of
500 the air-ocean exchange coefficient (K_g), and the influence of MBE is conditioned by the monsoon and the topography of
501 China. The prevailing southwest monsoon in July can thrust the marine air mass into the third step area (the offshore
502 continental shelf), and its influence area is wider due to the lack of obstacles in the north-south direction. However, in
503 January, April and October, the prevailing northerly monsoon brings more terrestrial air, limiting the influence of MBE. The
504 special geographical characteristics of some areas, e.g., Hainan Island, Fujian and Guangdong provinces etc., make them
505 more prone to the influence of the strong ocean air mass. Chla indirectly influences the calculation results of exchange flux
506 by affecting the calculation of pH. With the increase of Chla, exchange flux decreases sharply at first and then becomes
507 constant, and the ocean also transforms from a source of amines to a sink. In addition, the emission flux and spatial
508 distribution of AE, and wet deposition also affect the simulation of amines.



509 On the other hand, it should be noted that due to the limitation of the algorithm (e.g., Eq. (8)), the MBE established in this
510 study is only applicable to the North Pacific region. Additionally, the dependence on satellite data and corresponding
511 accuracy makes MBE uncertain, and the amount of data processing required also increases the difficulty and cost of
512 establishing an emission source inventory. Therefore, further studies are needed to establish a more accurate numerical
513 simulation for the amines.

514 **Author contribution**

515 **Competing interests**

516 The authors declare that they have no conflict of interest.

517 **Financial Support**

518 This work was funded by the National Natural Science Foundation of China (grant numbers 42121004, 41905107, 41905086,
519 41425020), Guangdong Innovative and Entrepreneurial Research Team Program (grant number 2016ZT06N263), and the
520 Special Fund Project for Science and Technology Innovation Strategy of Guangdong Province (grant number
521 2019B121205004), the Natural Science Foundation of Guangdong Province (grant number 2021A1515011248), Science and
522 Technology Projects in Guangzhou (grant number 202102080141), Natural Science Foundation of Tianjin City (grant
523 number 21YFSNSN00200), the AirQuip (High-resolution Air Quality Information for Policy) Project funded by the
524 Research Council of Norway, the Collaborative Innovation Center of Climate Change, Jiangsu Province, China, and the
525 high-performance computing platform of Jinan University.

526 **References**

- 527 Barsanti, K. C., McMurry, P. H., and Smith, J. N.: The potential contribution of organic salts to new particle growth, *Atmos.*
528 *Chem. Phys.*, 9, 2949-2957, <https://doi.org/10.5194/acp-9-2949-2009>, 2009.
- 529 Bergman, T., Laaksonen, A., Korhonen, H., Malila, J., Dunne, E. M., Mielonen, T., Lehtinen, K. E. J., Kuhn, T., Arola, A.,
530 and Kokkola, H.: Geographical and diurnal features of amine-enhanced boundary layer nucleation, *J. Geophys. Res.-*
531 *Atmos.*, 120, 9606-9624, <https://doi.org/10.1002/2015JD023181>, 2015.
- 532 Carl, S. A. and Crowley, J. N.: Sequential two (blue) photon absorption by NO₂ in the presence of H₂ as a source of OH in
533 pulsed photolysis kinetic studies: rate constants for reaction of OH with CH₃NH₂, (CH₃)₂NH, (CH₃)₃N, and C₂H₅NH₂ at
534 295 K, *J. Phys. Chem. A*, 102, 8131-8141, 1998.



- 535 Carpenter, L. J., Archer, S. D., and Beale, R.: Ocean-atmosphere trace gas exchange, *Chem. Soc. Rev.*, 41, 6473-6506,
536 <https://doi.org/10.1039/c2cs35121h>, 2012.
- 537 Chen, X., Situ, S., Zhang, Q., Wang, X., Sha, C., Zhou, L., Wu, L., Wu, L., Ye, L., and Li, C.: The synergetic control of
538 NO₂ and O₃ concentrations in a manufacturing city of southern China, *Atmos. Environ.*, 201, 402-416,
539 <http://dx.doi.org/10.1016/j.atmosenv.2018.12.021>, 2018.
- 540 Chen, D.H., Shen, Y.J., Wang, J.T., Gao, Y., Gao, H.W., Yao, X.H.: Mapping gaseous dimethylamine, trimethylamine,
541 ammonia, and their particulate counterparts in marine atmospheres of China's marginal seas - Part 1: Differentiating
542 marine emission from continental transport, *Atmos. Chem. Phys.*, 21(21), 16413-16425, [http://dx.doi.org/10.5194/acp-](http://dx.doi.org/10.5194/acp-21-16413-2021)
543 21-16413-2021, 2021.
- 544 Chen, D.H., Yao, X.H., Chan, C.K., Tian, X.M., Chu, Y.X., Clegg, S.L., Shen, Y.J., Gao, Y., Gao, H.W.: Competitive
545 Uptake of Dimethylamine and Trimethylamine against Ammonia on Acidic Particles in Marine Atmospheres, *Environ.*
546 *Sci. Technol.*, 56(9), 5430-5439, <http://dx.doi.org/10.1021/acs.est.1c08713>, 2022.
- 547 Cui, H., Chen, W., Dai, W., Liu, H., Wang, X., and He, K.: Source apportionment of PM_{2.5} in Guangzhou combining
548 observation data analysis and chemical transport model simulation, *Atmos. Environ.*, 116, 262-271,
549 <http://dx.doi.org/10.1016/j.atmosenv.2015.06.054>, 2015.
- 550 Duce, R. A., Liss, P. S., Merrill, J. T., Atlas, E. L., Buat - Menard, P., Hicks, B. B., Miller, J. M., Prospero, J. M., Arimoto,
551 R., Church, T. M., Ellis, W., Galloway, J. N., Hansen, L. J., Jickells, T. D., Knap, A. H., Reinhardt, K. H., Schneider, B.,
552 Soudine, A., Tokos, J. J., Tsunogai, S., Wollast, R., and Zhou, M.: The atmospheric input of trace species to the world
553 ocean, *Global Biogeochem. Cy.*, 5, 193-259, <https://doi.org/10.1029/91GB01778>, 1991.
- 554 Elm, J., Jen, C. N., Kurten, T., and Vehkamäki, H.: Strong hydrogen bonded molecular interactions between atmospheric
555 diamines and sulfuric acid, *J. Phys. Chem. A*, 120, 3693-3700, <https://doi.org/10.1021/acs.jpca.6b03192>, 2016.
- 556 Elm, J., Passananti, M., Kurten, T., and Vehkamäki, H.: Diamines can initiate new particle formation in the atmosphere, *J.*
557 *Phys. Chem. A*, 121, 6155-6164, <https://doi.org/10.1021/acs.jpca.7b05658>, 2017.
- 558 Gao, J., Chai, F. H., Wang, T., and Wang, W. X.: Particle number size distribution and new particle formation (NPF) in
559 Lanzhou, Western China, *Particuology*, 9, 611-618, <https://doi.org/10.1016/j.partic.2011.06.008>, 2011.
- 560 Gao, Y.T., Chen, D.H., Shen, Y.J., Gao, Y., Gao, H.W., Yao, X.H.: Mapping gaseous dimethylamine, trimethylamine,
561 ammonia, and their particulate counterparts in marine atmospheres of China's marginal seas - Part 2: Spatiotemporal
562 heterogeneity, causes, and hypothesis, *Atmos. Chem. Phys.*, 22(2), 1515-1528, [https://doi.org/10.5194/acp-22-1515-](https://doi.org/10.5194/acp-22-1515-2022)
563 2022, 2022.
- 564 Ge, X. L., Wexler, A. S., and Clegg, S. L.: Atmospheric amines - Part I. A review, *Atmos. Environ.*, 45, 524-546,
565 <https://doi.org/10.1016/j.atmosenv.2010.10.012>, 2011.
- 566 Gibb, S. W., Mantoura, R. F. C., and Liss, P. S.: Ocean-atmosphere exchange and atmospheric speciation of ammonia and
567 methylamines in the region of the NW Arabian Sea, *Global Biogeochem. Cy.*, 13, 161-177,
568 <https://doi.org/10.1029/98GB00743>, 1999.



- 569 Guenther, A., Karl, T., Harley, P., Wiedinmyer, C., Palmer, P. I., and Geron, C.: Estimates of global terrestrial isoprene
570 emissions using MEGAN (Model of Emissions of Gases and Aerosols from Nature), *Atmos. Chem. Phys.*, 6(1), 3181-
571 3210, <http://dx.doi.org/10.5194/acp-6-3181-2006>, 2006.
- 572 Hong, Y., Liu, Y. R., Wen, H., Miao, S. K., Huang, T., Peng, X. Q., Jiang, S., Feng, Y. J., and Huang, W.: Interaction of
573 oxalic acid with methylamine and its atmospheric implications, *RSC Adv.*, 8, 7225-7234,
574 <https://doi.org/10.1039/c7ra13670f>, 2018.
- 575 Hu, Q. J., Qu, K. M., Gao, H. W., Cui, Z. G., Gao, Y., and Yao, X. H.: Large increases in primary trimethylaminium and
576 secondary dimethylaminium in atmospheric particles associated with cyclonic eddies in the northwest Pacific Ocean, *J.*
577 *Geophys. Res. Atmos.*, 123, 12133-12146, <https://doi.org/10.1029/2018JD028836>, 2018.
- 578 Huang, R. J., Zhang, Y. L., Bozzetti, C., Ho, K. F., Cao, J. J., Han, Y. M., Daellenbach, K. R., Slowik, J. G., Platt, S. M.,
579 Canonaco, F., Zotter, P., Wolf, R., Pieber, S. M., Brun, E. A., Crippa, M., Ciarelli, G., Piazzalunga, A., Schwikowski,
580 M., Abbaszade, G., Schnelle-Kreis, J., Zimmermann, R., An, Z. S., Szidat, S., Baltensperger, U., El Haddad, I., and
581 Prevot, A. S. H.: High secondary aerosol contribution to particulate pollution during haze events in China, *Nature*, 514,
582 218-222, <https://doi.org/10.1038/nature13774>, 2014.
- 583 Kennedy, J., Morice, C., Parker, D., Kendon, M.: Global and regional climate in 2015, *Weather*, 71(8), 185-192,
584 <https://doi.org/10.1002/wea.2760>, 2016.
- 585 Khoo, K. H., Culberson, C. H., and Bates, R. G.: Thermodynamics of the dissociation of ammonium ion in seawater from 5
586 to 40°C, *J. Soln. Chem.*, 6, 281-290, 1977.
- 587 Kirkby, J., Curtius, J., Almeida, J., Dunne, E., Duplissy, J., Ehrhart, S., Franchin, A., Gagne, S., Ickes, L., Kurten, A., Kupc,
588 A., Metzger, A., Riccobono, F., Rondo, L., Schobesberger, S., Tsagkogeorgas, G., Wimmer, D., Amorim, A., Bianchi,
589 F., Breitenlechner, M., David, A., Dommen, J., Downard, A., Ehn, M., Flagan, R. C., Haider, S., Hansel, A., Hauser, D.,
590 Jud, W., Junninen, H., Kreissl, F., Kvashin, A., Laaksonen, A., Lehtipalo, K., Lima, J., Lovejoy, E. R., Makhmutov, V.,
591 Mathot, S., Mikkila, J., Minginette, P., Mogo, S., Nieminen, T., Onnela, A., Pereira, P., Petaja, T., Schnitzhofer, R.,
592 Seinfeld, J. H., Sipila, M., Stozhkov, Y., Stratmann, F., Tome, A., Vanhanen, J., Viisanen, Y., Virtala, A., Wagner, P. E.,
593 Walther, H., Weingartner, E., Wex, H., Winkler, P. M., Carslaw, K. S., Worsnop, D. R., Baltensperger, U., and Kulmala,
594 M.: Role of sulphuric acid, ammonia and galactic cosmic rays in atmospheric aerosol nucleation, *Nature*, 476, 429-U77,
595 <https://doi.org/10.1038/nature10343>, 2011.
- 596 Kulmala, M.: How particles nucleate and grow, *Science*, 302, 1000-1001, <https://doi.org/10.1126/science.1090848>, 2003.
- 597 Lian, X. F., Zhang, G. H., Lin, Q. H., Liu, F. X., Peng, L., Yang, Y. X., Fu, Y. Z., Jiang, F., Bi, X. H., Chen, D. H., Wang, X.
598 M., Peng, P. A., and Sheng, G. Y.: Seasonal variation of amine-containing particles in urban Guangzhou, China. *Atmos.*
599 *Environ*, 222, 117102, <https://doi.org/10.1016/j.atmosenv.2019.117102>, 2020.
- 600 Liss, P. S., and Slater, P. G.: Flux of gases across the air-sea interface, *Nature*, 147, 181-184,
601 <https://doi.org/10.1038/247181a0>, 1974.



- 602 Liu, F. X., Bi, X. H., Zhang, G. H., Lian, X. F., Fu, Y. Z., Yang, Y. X., Lin, Q. H., Jiang, F., Wang, X. M., Peng, P. A., and
603 Sheng, G. Y.: Gas-to-particle partitioning of atmospheric amines observed at a mountain site in southern China, *Atmos.*
604 *Environ.*, 195, 1-11, <https://doi.org/10.1016/j.atmosenv.2018.09.038>, 2018.
- 605 Liu, Y., Hong, Y., Fan, Q., Wang, X., Chan, P., Chen, X., Lai, A., Wang, M., and Chen, X. L.: Source-receptor relationships
606 for PM 2.5 during typical pollution episodes in the Pearl River Delta city cluster, China, *Sci. Total. Environ.*, 596-597,
607 194-206, <http://dx.doi.org/10.1016/j.scitotenv.2017.03.255>, 2017.
- 608 Loukonen, V., Kurten, T., Ortega, I. K., Vehkamäki, H., Padua, A. A. H., Sellegri, K., and Kulmala, M.: Enhancing effect of
609 dimethylamine in sulfuric acid nucleation in the presence of water - a computational study, *Atmos. Chem. Phys.*, 10,
610 4961-4974, <https://doi.org/10.5194/acp-10-4961-2010>, 2010.
- 611 Lyman, J., and Fleming, R. H.: Composition of seawater, *J. Mar. Res.*, 3, 134-136, 1940.
- 612 Ma, X. H., Sun, Y. H., Huang, Z. X., Zhang, Q. Z., and Wang, W. X.: A density functional theory study of the molecular
613 interactions between a series of amides and sulfuric acid, *Chemosphere*, 214, 781-790,
614 <https://doi.org/10.1016/j.chemosphere.2018.08.152>, 2019.
- 615 Mao, J. B., Yu, F. Q., Zhang, Y., An, J. Y., Wang, L., Zheng, J., Yao, L., Luo, G., Ma, W. C., Yu, Q., Huang, C., Li, L., and
616 Chen, L. M.: High-resolution modeling of gaseous methylamines over a polluted region in China: source-dependent
617 emissions and implications of spatial variations, *Atmos. Chem. Phys.*, 18, 7933-7950, [https://doi.org/10.5194/acp-18-](https://doi.org/10.5194/acp-18-7933-2018)
618 [7933-2018](https://doi.org/10.5194/acp-18-7933-2018), 2018.
- 619 Miao, S. K., Jiang, S., Peng, X. Q., Liu, Y. R., Feng, Y. J., Wang, Y. B., Zhao, F., Huang, T., and Huang, W.: Hydration of
620 the methanesulfonate-ammonia/amine complex and its atmospheric implications, *RSC Adv.*, 8, 3250-3263,
621 <https://doi.org/10.1039/c7ra12064h>, 2018.
- 622 Myriokefalitakis, S., Vignati, E., Tsigaridis, K., Papadimas, C., Sciare, J., Mihalopoulos, N., Facchini, M. C., Rinaldi, M.,
623 Dentener, F. J., Ceburnis, D., Hatzianastasiou, N., O'Dowd, C. D., van Weele, M., and Kanakidou, M.: Global modeling
624 of the oceanic source of organic aerosols, *Adv. Meteorol.*, <https://doi.org/10.1155/2010/939171>, 2010.
- 625 Nakano, Y., and Watanabe, Y. W.: Reconstruction of pH in the surface seawater over the north pacific basin for all seasons
626 using temperature and chlorophyll-a, *J. Oceanogr.*, 61, 673-680. <https://doi.org/10.1007/s10872-005-0075-6>, 2005.
- 627 Qiu, C., and Zhang, R. Y.: Multiphase chemistry of atmospheric amines, *Phys. Chem. Chem. Phys.* 15, 5738-5752,
628 <https://doi.org/10.1039/c3cp43446j>, 2013.
- 629 Qiu, C., Wang, L., Lal, V., Khalizov, A. F., and Zhang, R. Y.: Heterogeneous reactions of alkylamines with ammonium
630 sulfate and ammonium bisulfate, *Environ. Sci. Technol.*, 45, 4748-4755, <https://doi.org/10.1021/es1043112>, 2011.
- 631 Smith, J. N., Barsanti, K. C., Friedli, H. R., Ehn, M., Kulmala, M., Collins, D. R., Scheckman, J. H., Williams, B. J., and
632 McMurry, P. H.: Observations of aminium salts in atmospheric nanoparticles and possible climatic implications, *Proc.*
633 *Natl. Acad. Sci. U. S. A.*, 107, 6634-6639, <https://doi.org/10.1073/pnas.0912127107>, 2010.



- 634 Smith, J. N., Dunn, M. J., VanReken, T. M., Iida, K., Stolzenburg, M. R., McMurry, P. H., and Huey, L. G.: Chemical
635 composition of atmospheric nanoparticles formed from nucleation in Tecamac, Mexico: Evidence for an important role
636 for organic species in nanoparticle growth, *Geophys. Res. Lett.*, 35, <https://doi.org/10.1029/2007GL032523>, 2008.
- 637 Van Neste, A., Duce, R. A., and C. Lee: Methylamines in the marine atmosphere, *Geophys. Res. Lett.*, 14, 711-714, 1987.
- 638 Waller, S. E., Yang, Y., Castracane, E., Racow, E. E., Kreinbihl, J. J., Nickson, K. A., and Johnson, C. J.: The interplay
639 between hydrogen bonding and coulombic forces in determining the structure of sulfuric acid-amine clusters, *J. Phys.
640 Chem. Lett.*, 9, 1216-1222, <https://doi.org/10.1021/acs.jpcclett.8b00161>, 2018.
- 641 Wang, C. Y., Jiang, S., Liu, Y. R., Wen, H., Wang, Z. Q., Han, Y. J., Huang, T., and Huang, W.: Synergistic effect of
642 ammonia and methylamine on nucleation in the earth's atmosphere: A theoretical study, *J. Phys. Chem. A*, 122, 3470-
643 3479, <https://doi.org/10.1021/acs.jpca.8b00681>, 2018.
- 644 Wang, D. F., Zhou, B., Fu, Q. Y., Zhao, Q. B., Zhang, Q., Chen, J. M., Yang, X., Duan, Y. S., and Li, J.: Intense secondary
645 aerosol formation due to strong atmospheric photochemical reactions in summer: observations at a rural site in eastern
646 Yangtze River Delta of China, *Sci. Total Environ.*, 571, 1454-1466, <https://doi.org/10.1016/j.scitotenv.2016.06.212>,
647 2017.
- 648 Wang, D. W., Guo, H., Cheung, K., and Gan, F. X.: Observation of nucleation mode particle burst and new particle
649 formation events at an urban site in Hong Kong, *Atmos. Environ.*, 99, 196-205,
650 <https://doi.org/10.1016/j.atmosenv.2014.09.074>, 2014.
- 651 Wilemski, G.: Composition of the critical nucleus in multicomponent vapor nucleation, *J. Chem. Phys.*, 80,
652 <https://doi.org/10.1063/1.446822>, 1983.
- 653 Wu, Z. J., Ma, N., Gross, J., Kecorius, S., Lu, K. D., Shang, D. J., Wang, Y., Wu, Y. S., Zeng, L. M., Hu, M., Wiedensohler,
654 A., and Zhang, Y. H.: Thermodynamic properties of nanoparticles during new particle formation events in the
655 atmosphere of North China Plain, *Atmos. Res.*, 188, 55-63, <https://doi.org/10.1016/j.atmosres.2017.01.007>, 2017.
- 656 Xiao, Q., Li, M., Liu, H., Fu, M. L., Deng, F. Y., Lv, Z. F., Man, H. Y., Jin, X. X., Liu, S., and He, K. B.: Characteristics of
657 marine shipping emissions at berth: profiles for particulate matter and volatile organic compounds, *Atmos. Chem. Phys.*,
658 18, 9527-9545, <https://doi.org/10.5194/acp-18-9527-2018>, 2018.
- 659 Xiao, S., Wang, M. Y., Yao, L., Kulmala, M., Zhou, B., Yang, X., Chen, J. M., Wang, D. F., Fu, Q. Y., Worsnop, D. R., and
660 Wang, L.: Strong atmospheric new particle formation in winter in urban Shanghai, China, *Atmos. Chem. Phys.*, 15,
661 1769-1781, <https://doi.org/10.5194/acp-15-1769-2015>, 2015.
- 662 Xie, H., Feng, L. M., Hu, Q. J., Zhu, Y. J., Gao, H. W., Gao, Y., and Yao, X. H.: Concentration and size distribution of
663 water-extracted dimethylammonium and trimethylammonium in atmospheric particles during nine campaigns - Implications
664 for sources, phase states and formation pathways, *Sci. Total Environ.*, 631-632, 130-141,
665 <https://doi.org/10.1016/j.scitotenv.2018.02.303>, 2018.
- 666 Yao, L., Garmash, O., Bianchi, F., Zheng, J., Yan, C., Kontkanen, J., Junninen, H., Mazon, S. B., Ehn, M., Paasonen, P.,
667 Sipila, M., Wang, M. Y., Wang, X. K., Xiao, S., Chen, H. F., Lu, Y. Q., Zhang, B. W., Wang, D. F., Fu, Q. Y., Geng, F.



- 668 H., Li, L., Wang, H. L., Qiao, L. P., Yang, X., Chen, J. M., Kerminen, V. M., Petaja, T., Worsnop, D. R., Kulmala, M.,
669 and Wang, L.: Atmospheric new particle formation from sulfuric acid and amines in a Chinese megacity, *Science*, 361,
670 278-+, <https://doi.org/10.1126/science.aao4839>, 2018.
- 671 Yao, L., Wang, M. Y., Wang, X. K., Liu, Y. J., Chen, H. F., Zheng, J., Nie, W., Ding, A. J., Geng, F. H., Wang, D. F., Chen,
672 J. M., Worsnop, D. R., and Wang, L.: Detection of atmospheric gaseous amines and amides by a high-resolution time-
673 of-flight chemical ionization mass spectrometer with protonated ethanol reagent ions, *Atmos. Chem. Phys.*, 16, 14527-
674 14543, <https://doi.org/10.5194/acp-16-14527-2016>, 2016.
- 675 Yu, F., and Luo, G.: Modeling of gaseous methylamines in the global atmosphere: impacts of oxidation and aerosol uptake,
676 *Atmos. Chem. Phys.*, 14, 12455-12464, <https://doi.org/10.5194/acp-14-12455-2014>, 2014.
- 677 Yu, F.: A secondary organic aerosol formation model considering successive oxidation aging and kinetic condensation of
678 organic compounds: global scale implications, *Atmos. Chem. Phys.*, 11, 1083-1099, <https://doi.org/10.5194/acp-11-1083-2011>, 2011.
- 680 Zhang, R. Y., Wang, G. H., Guo, S., Zarnora, M. L., Ying, Q., Wang, W. G., Hu, M., and Wang, Y.: Formation of Urban
681 Fine Particulate Matter, *Chem. Rev.*, 115, 3803-3855, <https://doi.org/10.1021/acs.chemrev.5b00067>, 2015.
- 682 Zheng, J., Ma, Y., Chen, M. D., Zhang, Q., Wang, L., Khalizov, A. F., Yao, L., Wang, Z., Wang, X., and Chen, L. X.:
683 Measurement of atmospheric amines and ammonia using the high resolution time-of-flight chemical ionization mass
684 spectrometry, *Atmos. Environ.*, 102, 249-259, <https://doi.org/10.1016/j.atmosenv.2014.12.002>, 2015.
- 685 Zhou, S. Q., Li, H. W., Yang, T. J., Chen, Y., Deng, C. R., Gao, Y. H., Chen, C. P., and Xu, J.: Characteristics and sources
686 of aerosol aminiums over the eastern coast of China: insights from the integrated observations in a coastal city, adjacent
687 island and surrounding marginal seas, *Atmos. Chem. Phys.*, 19, 10447-10467, <https://doi.org/10.5194/acp-19-10447-2019>, 2019.



689 Table 1 Amines-to-ammonia mass emission ratios (Mao et al., 2018)

| | Transportation Emissions | Residential Emissions | Other industrial Emissions | Chemical industrial Emissions (Power Plant) | Agricultural Emissions |
|-----|--------------------------|-----------------------|----------------------------|---------------------------------------------|------------------------|
| MA | 0.0011 | 0.0011 | 0.0015 | 0.026 | 0.0011 |
| DMA | 0.00090 | 0.010 | 0.0018 | 0.0070 | 0.0015 |
| TMA | 0.00040 | 0.00060 | 0.00050 | 0.00040 | 0.00040 |

690



691 Table 2 Configuration of WRF-Chem parameterization schemes

| Physical parameterization schemes | | Chemical parameterization schemes | |
|-----------------------------------|--------------------------------------------------------------|--------------------------------------------|--------------------------------------------------------------------------------------------------------------------------------------------------------------------------------------------------------------|
| mp_physics=11 | CAM5 Morrison-Gettleman scheme to be used with MAM chemistry | chem_opt=503 | CBMZ with CAM-MAM3_AQ |
| bl_pbl_physics = 9 | CAM5 UW PBL scheme to be used with CAM-MAM chemistry | emiss_inpt_opt=104 | Carbon Bond 4-emission speciation adapted after reading the RADM2 data file. Secondary Organic Aerosol (SOA) precursors computed from input data as well. Using for CAM5 microphysics and MAM 3-mode aerosol |
| cu_physics = 7 | CAM5 Zhang-McFarlane scheme to be used with MAM chemistry | emiss_inpt_opt=9 | Converting default RADM2 gas emissions to CBMZ. Aerosol emissions are speciated to MAM 3-mode aerosols |
| | | cam_mam_mode = 3 | Number of MAM aerosol modes |
| | | cam_mam_nspec = 88 (original value: 85) | Number of MAM 3-bin aerosol species |

692



693 Table 3. A brief summary of previous research results on the distribution of amines.

| Location | Site Type | Period | [NH ₃ (g)] (pmol m ⁻³) | [MMA(g)] (pmol m ⁻³) | [DMA(g)] (pmol m ⁻³) | [TMA(g)] (pmol m ⁻³) | [NH ₃ (s) tot ⁺] (μmol m ⁻³) | [MMA(s) tot ⁺] (μmol m ⁻³) | [DMA(s) tot ⁺] (μmol m ⁻³) | [TMA(s) tot ⁺] (μmol m ⁻³) | Ref. |
|-------------------------------|----------------|-----------------------------------------|--------------------------------------------------|-------------------------------------|-------------------------------------|-------------------------------------|-----------------------------------------------------------------------|----------------------------------------------------------|----------------------------------------------------------|----------------------------------------------------------|----------------------------------|
| Oahu, Hawaii | Coast | July–August 1985 | - | 11±5 | 93±51 | 30±19 | - | 52±20 | 1.5±20 | 12±3 | Van Neste et al. (1987) |
| Narragansett, Rhode Island | Coast | | - | 52±12 | 240±40 | 100±40 | - | | | | |
| Vineyard S. | Coast | | - | | | | - | 200±58 | 8.9±4.4 | 41±27 | |
| Salt Pond | Coast | | | | | | | 32±5 | 8.9±1.1 | 10±13 | |
| Arabian Sea | Arabian Sea | 27 August– 4 October 1994 | 946 | 114 | 39 | 0.9 | 108 | 16.2 | 4.54 | 0.044 | Gibb et al. (1999) |
| Arabian Sea | Arabian Sea | 16 November - 19 December 1994 | 3780 | 143 | 196 | 8.1 | 156 | 25.6 | 4.85 | 0.14 | |

694



695 Table 4 Physicochemical parameters used in flux calculations.

| Variable (Units) | Species | | | References |
|-----------------------------------------------------------------------------------------|---------|--------|--------|--------------------|
| | MMA | DMA | TMA | |
| MW (g mol ⁻¹) | 31.06 | 45.12 | 59.11 | |
| Henry's law constant, H (T=20 °C, I=0 mol dm ⁻³) | 0.0015 | 0.0013 | 0.0023 | |
| Thermodynamic stability constant, pK _{wα} (T=20 °C, I=0 mol dm ⁻³) | 10.64 | 10.77 | 9.80 | Gibb et al. (1999) |
| K _H (M atm ⁻¹) | 23.80 | 27.47 | 15.53 | |

696



697 Table 5 Emission fluxes of the three types of amines in January, April, July and October.

| Site | Date | MMA ($\text{pmol m}^{-2} \text{s}^{-1}$) | DMA ($\text{pmol m}^{-2} \text{s}^{-1}$) | TMA ($\text{pmol m}^{-2} \text{s}^{-1}$) | Ref. |
|----------------------------------|-----------|--------------------------------------------|--------------------------------------------|--------------------------------------------|-------------------------|
| Eastern China | Jan. 2015 | -1.7 ± 0.37 | 0.85 ± 0.15 | -4.9 ± 1.0 | This study |
| | Apr. 2015 | -1.3 ± 0.41 | 0.70 ± 0.19 | -4.0 ± 2.1 | |
| | Jul. 2015 | -1.1 ± 0.35 | 0.58 ± 0.19 | -3.3 ± 1.0 | |
| | Oct. 2015 | -1.4 ± 0.36 | 0.74 ± 0.16 | -4.2 ± 1.0 | |
| Coastal Hawaii and Massachusetts | - | $-1.8 - -0.11$ | $0.46 - 0.49$ | $-3.2 - -0.20$ | Van Neste et al. (1987) |

698



699 Table 6 Comparison of gaseous methylamines from simulations and measurement results in different locations.

| Location (Site Type) | Data Type | Season | MMA (pptv) | DMA (pptv) | TMA (pptv) | Ref. |
|-----------------------------------------------|-------------------------|-------------|------------|-----------------------------|------------------------------|---------------------|
| Nanjing, China (Industrialized) | Measured | Summer | 0.1-18.9 | 0.1-29.9 | 0.1-9.3 | Zheng et al. (2015) |
| Shanghai, China (Urban) | Measured | Summer | 15.7±5.9 | 40.0±14.3 | 1.1±0.6 | Yao et al. (2016) |
| Shanghai, China (Urban) | Measured | Spring | - | 4.7-26.1 | - | Yao et al. (2018) |
| | | Summer | - | 27.1-81.7 | - | |
| | | Autumn | - | 19.9-27.3 | - | |
| Shanghai, China (Urban) | Measured | Winter | - | 3.5-16.7 | - | Mao et al. (2018) |
| | | Summer | 15.71 | 40.20 | 1.13 | |
| Nanjing, China (Urban) | Simulated | | 4.97±6.61 | 16.33±25.15 | 1.01±1.37 | Mao et al. (2018) |
| | Measured | Summer | 4.35 | 7.08 | 1.91 | |
| Nanjing, China (Urban) | Simulated | | 6.39 | 10.56 | 1.12 | Liu et al. (2018) |
| | Measured | Summer | 51.9±58.0 | 111.3±82.3 | - | |
| Nanling Mountain, southern China (Background) | Measured | Autumn | 56.1±32.4 | 45.5±34.7 | - | Liu et al. (2018) |
| | | Winter | - | 0.006 ± 0.006 | 12±4 | |
| Bohai Sea and Yellow Sea (Marine) | Measured | Winter | - | 0.002±0.011 | 14±5 | Gao et al. (2022) |
| The Yellow Sea (Marine) | Measured | Winter | - | 0.012±0.011 | 8-91 (26 ± 17) | Chen et al. (2021) |
| East China Sea (Marine) | Measured | Winter | - | 0.018±0.021 | 0.5 ng m ⁻³ | |
| The Yellow Sea and Bohai Sea (Marine) | Measured | Winter | - | 11 ± 6.5 ng m ⁻³ | 5.4 ± 2.4 ng m ⁻³ | Chen et al. (2022) |
| the coastline of eastern China (Marine) | Measured | Spring | - | 5.83±4.42 | 1.03±0.75 | This study |
| | | Summer | 5.15±3.79 | 5.83±4.42 | 1.03±0.75 | |
| | | Autumn | 6.79±4.27 | 7.07±4.41 | 1.34±0.83 | |
| | Simulated (Without MBE) | Winter | 18.01±8.76 | 21.85±10.94 | 3.59±1.75 | |
| | | Spring | 10.64±5.94 | 17.82±10.90 | 2.24±1.25 | |
| | Simulated (With MBE) | Summer | 5.22±3.78 | 5.84±4.41 | 1.57±1.07 | |
| | | Winter | 7.25±4.56 | 7.51±4.71 | 2.50±1.60 | |
| Autumn | 18.16±8.77 | 21.99±10.96 | 5.03±2.22 | | | |
| Winter | 10.67±5.95 | 17.71±10.94 | 2.72±1.51 | | | |



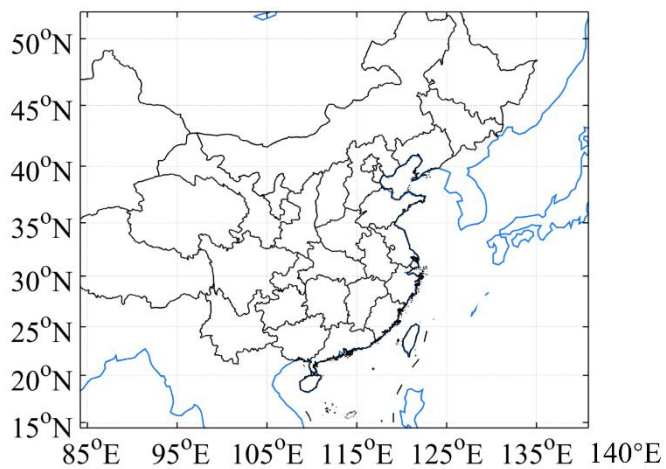
701 Table 7 Changes in methylamine concentrations with MBE contribution (Unit: %).

| | MMA | | | DMA | | | TMA | | |
|-----|-----------------|-----------------|-----------------|-----------------|-----------------|-----------------|-----------------|-----------------|-----------------|
| | MD ^a | MI ^b | MA ^c | MD ^a | MI ^b | MA ^c | MD ^a | MI ^b | MA ^c |
| Jan | -1.2 | 4.0 | 2.7 | -1.4 | 1.5 | 1.4 | -1.1 | 37.1 | 22.9 |
| Apr | -1.9 | 3.7 | 2.8 | -2.1 | 2.6 | 2.3 | -1.8 | 23.7 | 14.1 |
| Jul | -3.9 | 7.8 | 5.9 | -4.1 | 6.2 | 5.1 | -4.0 | 36.5 | 22.0 |
| Oct | -2.3 | 3.6 | 7.5 | -2.4 | 2.2 | 2.3 | -2.5 | 27.9 | 16.7 |

702 ^a The mean amplitude of the region where the concentration decreased.

703 ^b The mean amplitude of the region where the concentration increased.

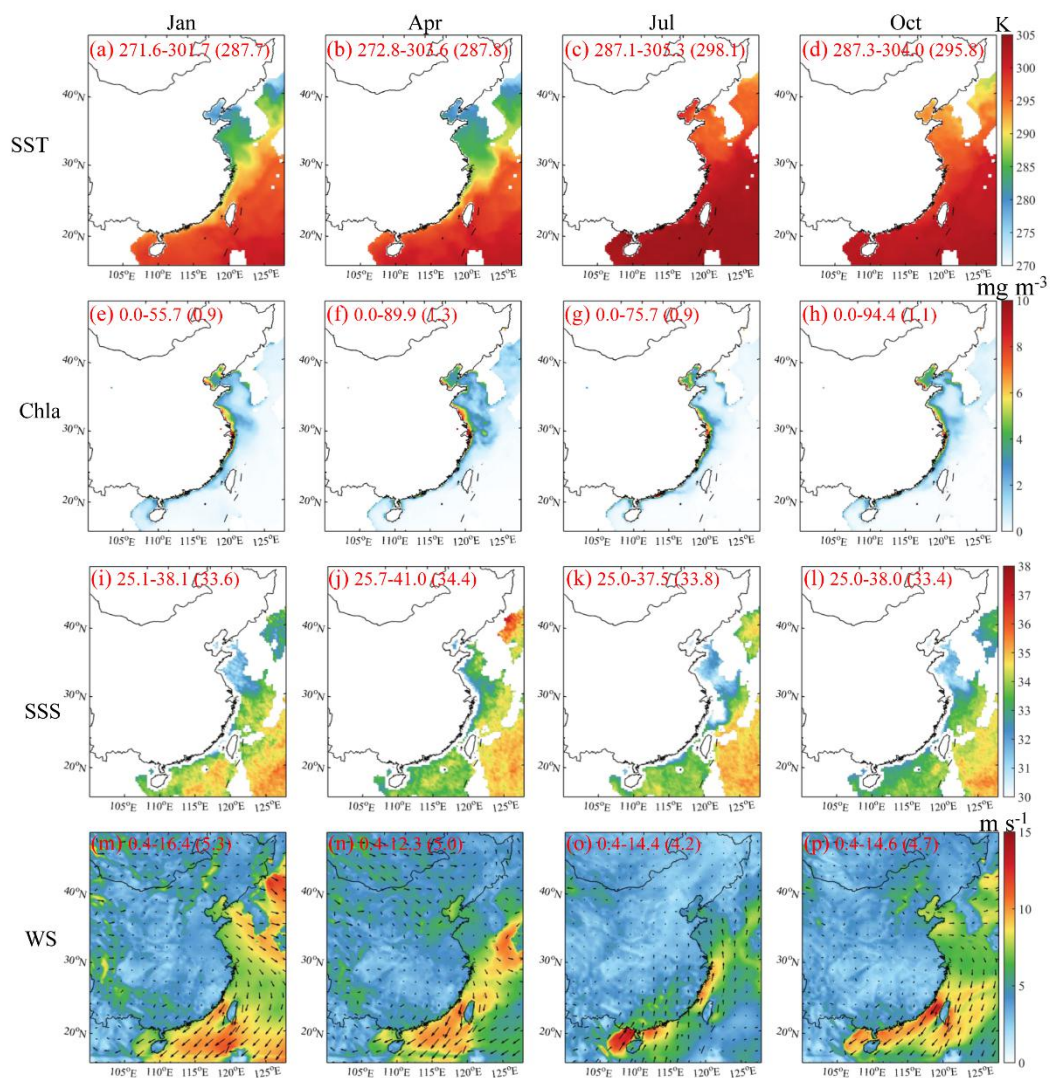
704 ^c Mean change in absolute concentration.



705

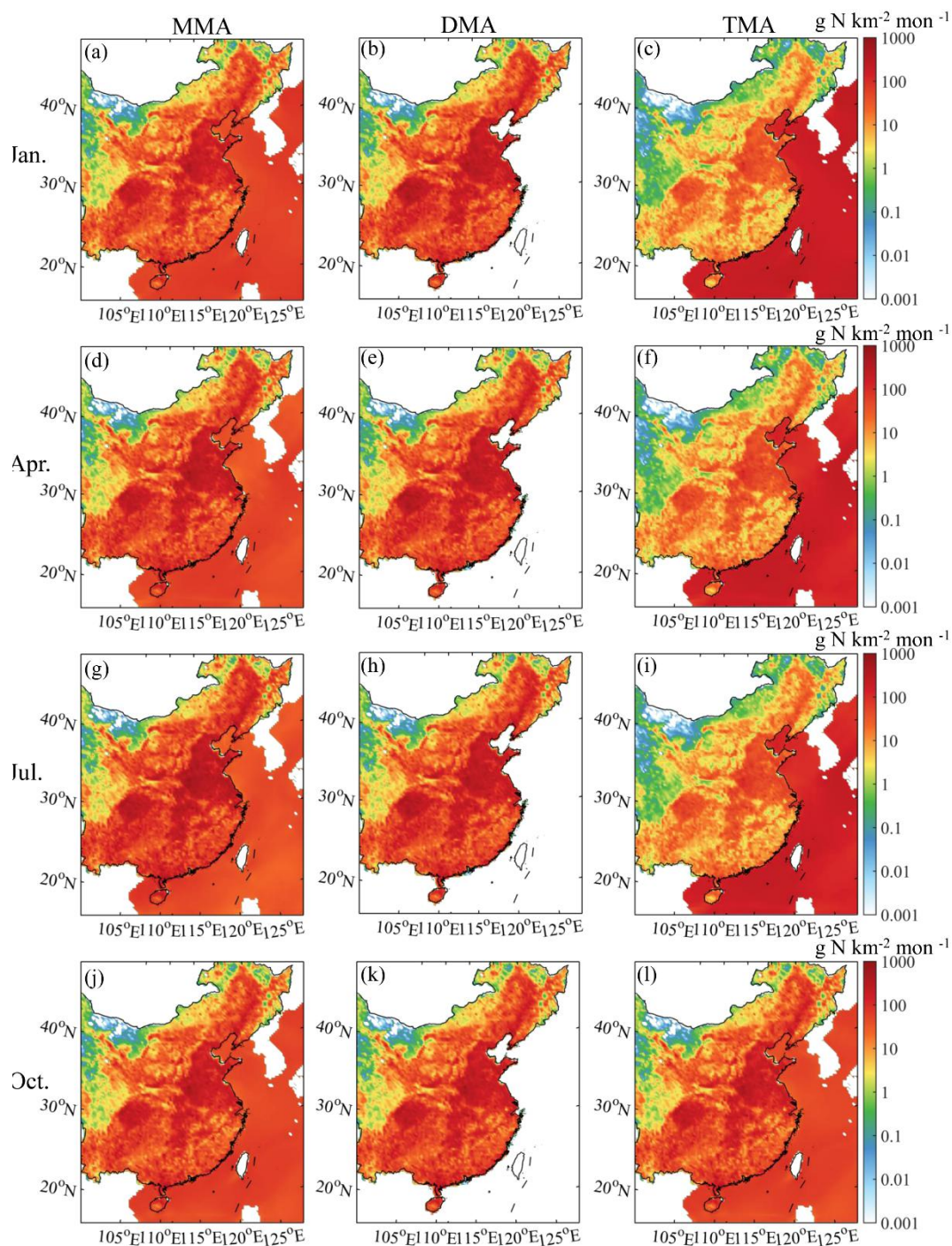
706

Figure 1: Simulation domain in this study.



707

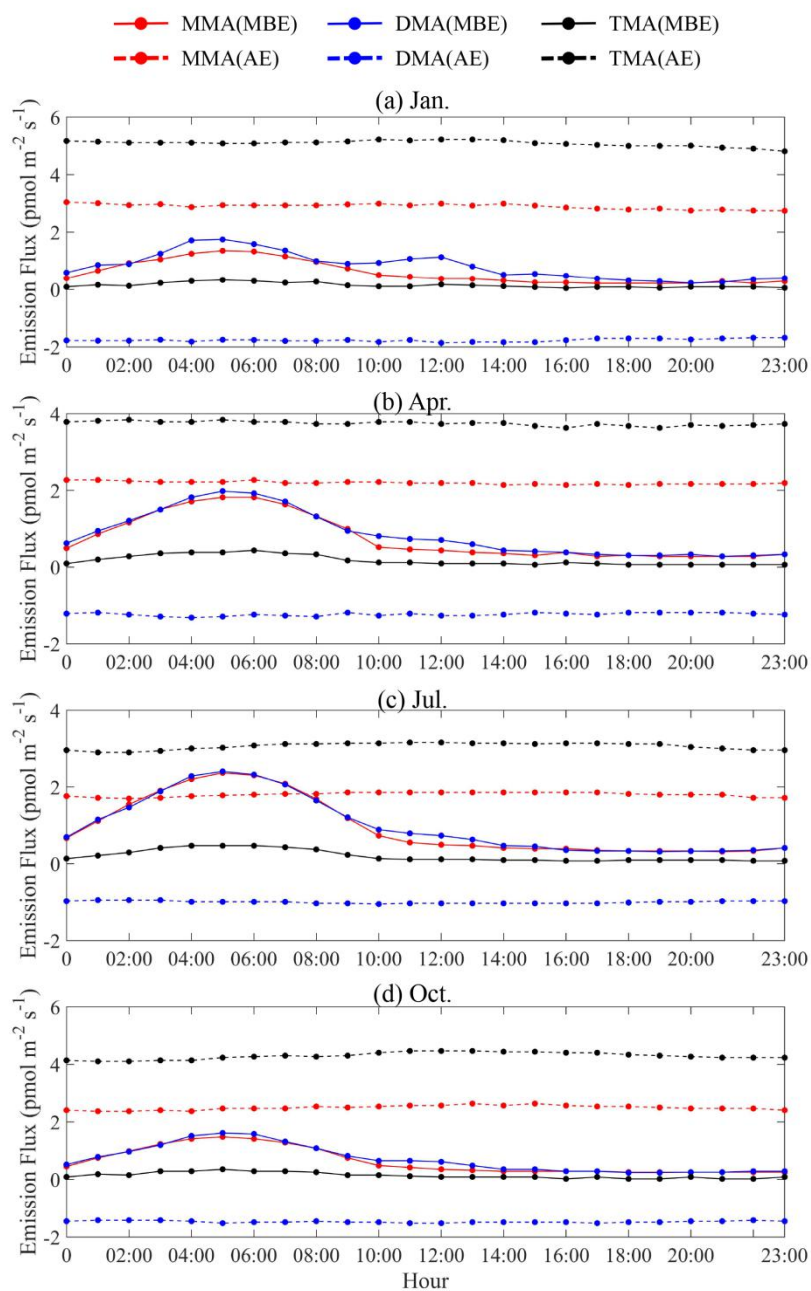
708 **Figure 2: Temporal and spatial distribution of SST (a-d), Chla (e-h), SSS (i-l), and WS (m-p) in January, April, July, and October.**
 709 **The numbers marked next to the serial number are the minimum, maximum, and average values from left to right.**



710

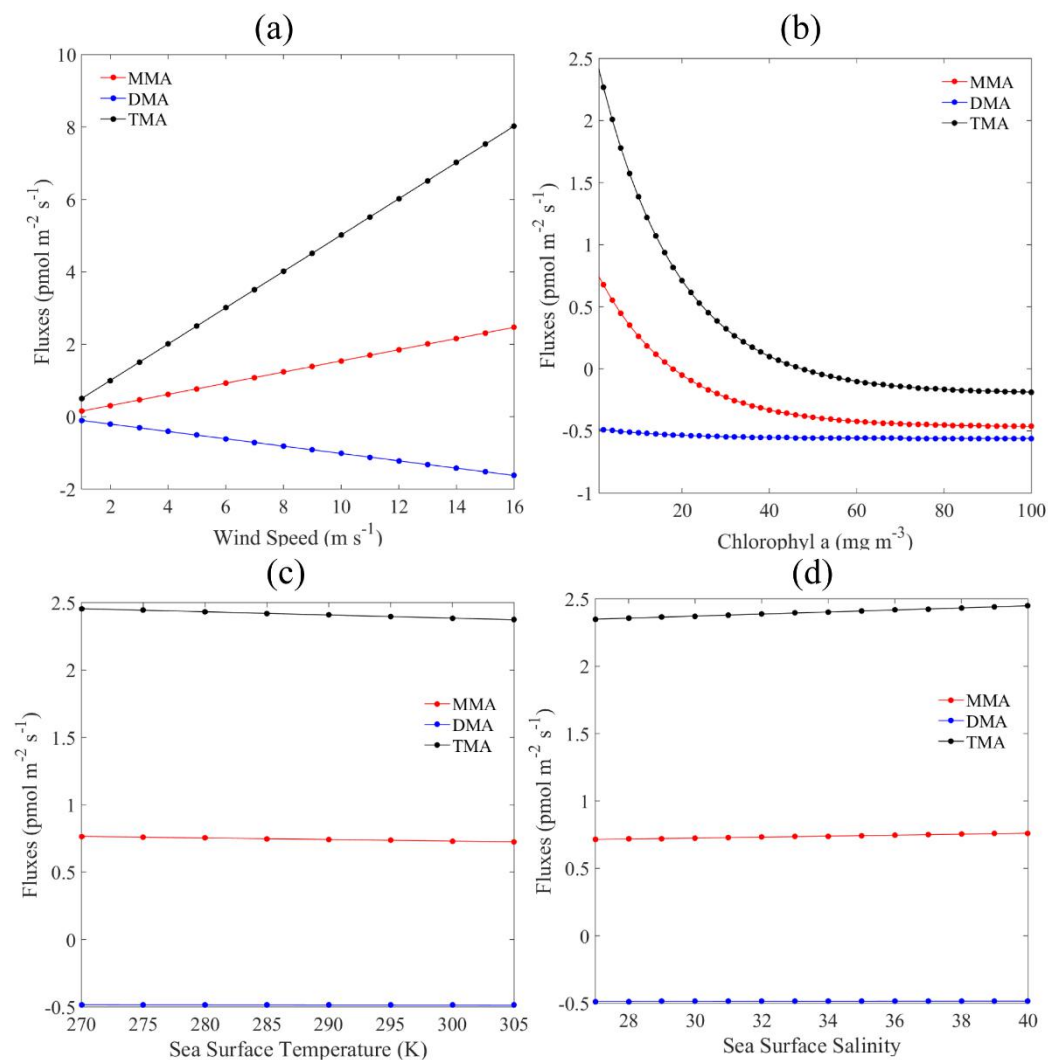
711 **Figure 3: Spatial and temporal distribution of methylamines emissions: (a, e, h, k) MMA; (b, f, l, l) DMA; (c, g, j, m)TMA.**

712



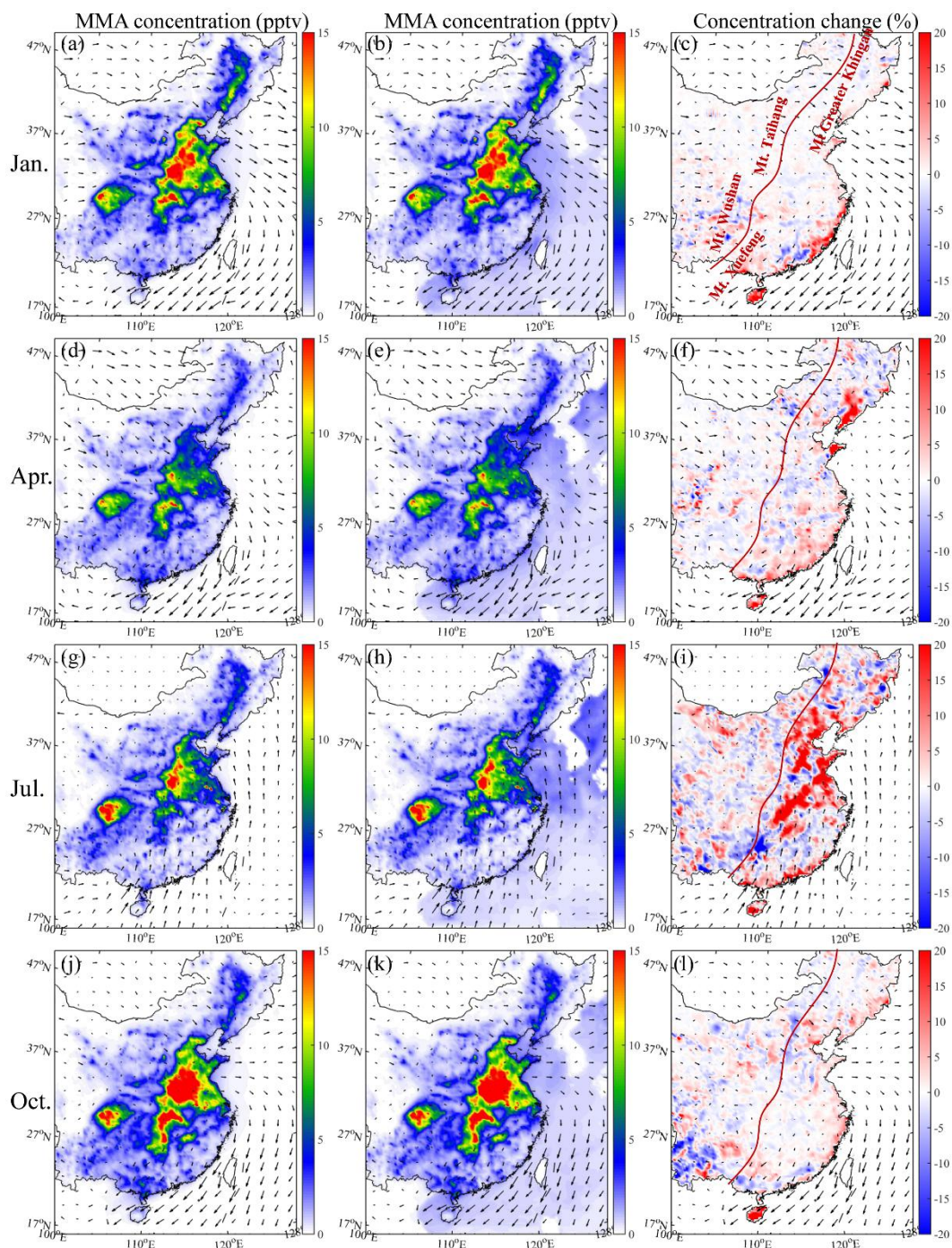
713

714 **Figure 4: Diurnal variation of emission fluxes of methylamines. (a) Jan. (b) Apr. (c) Jul. (d) Oct. The solid lines represent the**
715 **contribution from AE, the dotted lines represent the contribution from MBE.**



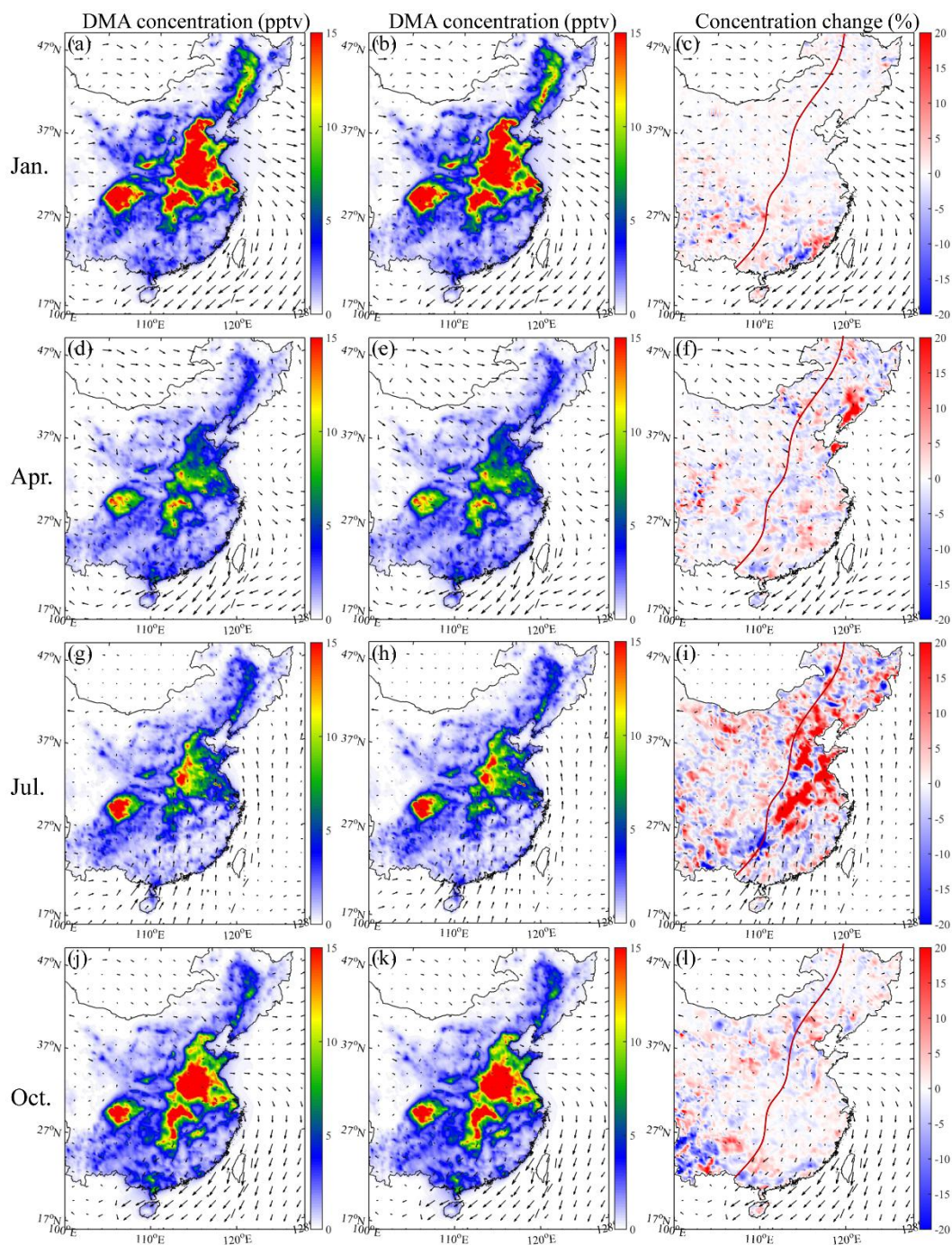
716

717 **Figure 5: Influence of WS, Chla, SSS and SST on amines exchange fluxes.**



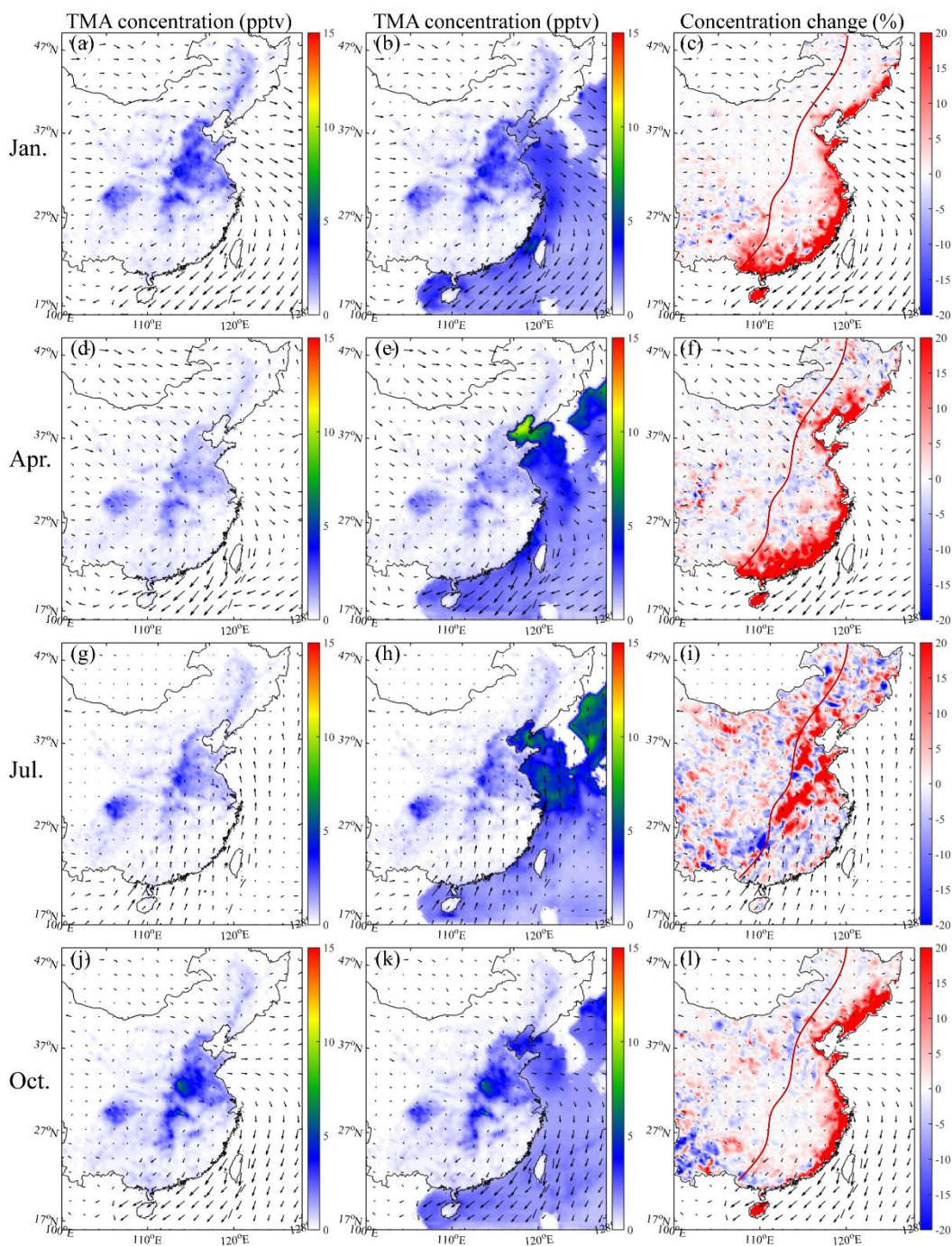
718

719 **Figure 6: Spatial and temporal distribution of MMA simulated concentration. (a) (e) (h) (k): Without MBE (Unit: pptv). (b) (f) (i)**
 720 **(l): With MBE (Unit: pptv). (c) (g) (j) (m): MMA concentration changes on land (Unit: %). The solid red line represents the**
 721 **boundary between the second and third steps of the Chinese terrain.**



722

723 **Figure 7: Spatial and temporal distribution of DMA simulated concentration. (a) (e) (h) (k): Without MBE (Unit: pptv). (b) (f) (i)**
724 **(l): With MBE (Unit: pptv). (c) (g) (j) (m): DMA concentration changes on land (Unit: %). The solid red line represents the**
725 **boundary between the second and third steps of the Chinese terrain.**



726
 727
 728
 729

Figure 8: Spatial and temporal distribution of TMA simulated concentration. (a) (e) (h) (k): Without MBE (Unit: pptv). (b) (f) (i) (l): With MBE (Unit: pptv). (c) (g) (j) (m): TMA concentration changes on land (Unit: %). The solid red line represents the boundary between the second and third steps of the Chinese terrain.